A Mechanism for the Auto-inhibition of Hyperpolarization-activated Cyclic Nucleotide-gated (HCN) Channel Opening and Its Relief by cAMP*

Madoka Akimoto[‡], **Zaiyong Zhang**[§], **Stephen Boulton**[¶], **Rajeevan Selvaratnam**[‡], **Bryan VanSchouwen**[‡], **Melanie Gloyd**[‡¶], **Eric A. Accili**[||1], **Oliver F. Lange**[§**], and **Giuseppe Melacini**[‡¶2]

From the Departments of [‡]Chemistry and Chemical Biology and [¶]Biochemistry and Biomedical Sciences, McMaster University, Hamilton, Ontario L8S 4M1, Canada, the [§]Biomolecular NMR and Munich Center for Integrated Protein Science, Department of Chemie, Technische Universität München, Lichtenbergstrasse 4, 85747 Garching, Germany, the [||]Department of Cellular and Physiological Sciences, University of British Columbia, Vancouver, British Columbia V6T 1Z3, Canada, and the [**]Institute of Structural Biology, Helmholtz Zentrum München, 85764 Neuherberg, Germany

Background: Hyperpolarization-activated cyclic nucleotide-gated (HCN) channels control electrical activity through tetramerization of an intracellular linker.
Results: NMR shows that the apo-cAMP-binding domain (CBD) of HCN4 destabilizes the tetramer through steric clashes.
Conclusion: The apo-HCN4 CBD structure is compatible with monomeric and dimeric but not with tetrameric HCN4.
Significance: The proposed mechanism explains HCN auto-inhibition and its relaxation by cAMP.

Hyperpolarization-activated cyclic nucleotide-gated (HCN) ion channels control neuronal and cardiac electrical rhythmicity. There are four homologous isoforms (HCN1–4) sharing a common multidomain architecture that includes an N-terminal transmembrane tetrameric ion channel followed by a cytoplasmic "C-linker," which connects a more distal cAMP-binding domain (CBD) to the inner pore. Channel opening is primarily stimulated by transmembrane elements that sense membrane hyperpolarization, although cAMP reduces the voltage required for HCN activation by promoting tetramerization of the intracellular C-linker, which in turn relieves auto-inhibition of the inner pore gate. Although binding of cAMP has been proposed to relieve auto-inhibition by affecting the structure of the C-linker and CBD, the nature and extent of these cAMP-dependent changes remain limitedly explored. Here, we used NMR to probe the changes caused by the binding of cAMP and of cCMP, a partial agonist, to the apo-CBD of HCN4. Our data indicate that the CBD exists in a dynamic two-state equilibrium, whose position as gauged by NMR chemical shifts correlates with the $V_{1/2}$ voltage measured through electrophysiology. In the absence of cAMP, the most populated CBD state leads to steric clashes with the activated or "tetrameric" C-linker, which becomes energetically unfavored. The steric clashes of the apo tetramer are eliminated either by cAMP binding, which selects for a CBD state devoid of steric clashes with the tetrameric C-linker and facilitates channel opening, or by a transition of apo-HCN to monomers or dimer of dimers, in which the C-linker becomes less structured, and channel opening is not facilitated.

Hyperpolarization-activated cyclic nucleotide-gated (HCN)[3] ion channels contribute to electrical activity in neurons and cardiomyocytes (1–22). Four homologous mammalian HCN variants are known to date (HCN1–4) that share a similar multidomain organization with an N-terminal transmembrane region and a C-terminal intracellular region (IR) (1). As for closely related voltage-gated potassium channels, the HCN transmembrane region is thought to form a tetrameric ion channel, with each subunit of the tetramer composed of six helices. The IR includes a linker with six additional helices (A′–F′ or "C-linker") that connect the transmembrane region to a C-terminal cAMP-binding domain (CBD) (Fig. 1, *a* and *b*) (1). Although HCN channels are primarily activated by hyperpolarization of the membrane potential, their opening is variably facilitated by cAMP binding to the CBD, with HCN2 and HCN4 responding strongly to cAMP, HCN1 responding to a lesser extent, and HCN3 being unaffected by cAMP (1–4) or exhibiting a negative cAMP-dependent shift in the half-maximal activation voltage (18). The cAMP-dependent modulation of HCN4 activity is a key determinant for the increased heart rate induced by β-adrenergic agonists (3, 4). This is because in the absence of cAMP the CBD causes a tonic inhibition of the HCN channel (21, 23), and binding of cAMP to the CBD relaxes the inhibition of the inner gate, so that opening by hyperpolarization occurs more easily (21–23).

The crystal structures of the cAMP-bound (holo) IR have been solved for HCN1, -2, and -4 (Fig. 1*c*) (1, 21, 22). No signif-

---

[1] Recipient of a Tier 2 Canada Research Chair.
[2] To whom correspondence should be addressed. E-mail: melacin@mcmaster.ca.

[3] The abbreviations used are: HCN, hyperpolarization-activated cyclic nucleotide-modulated; CBD, cyclic AMP-binding domain; EPAC, exchange protein directly activated by cAMP; HN-NOE, proton nitrogen-nuclear Overhauser effect; HSQC, heteronuclear single quantum coherence; PRE, paramagnetic relaxation enhancement; RDC, residual Dipolar coupling; STD, saturation transfer difference; SEC, size exclusion chromatography; r.m.s.d., root mean square deviation; IR, intracellular region; TD, tetramerization domain; CCS, compounded chemical shift; PDB, Protein Data Bank; MTSL, 1-oxyl-2,2,5,5-tetramethylpyrroline-3-methyl-methanethiosulfonate; eCBD, extended CBD; PBC, phosphate-binding cassette.

icant differences have been observed among the secondary, tertiary, and quaternary structures of the holo-IR for these HCN isoforms, which assemble to form a highly conserved homotetramer with a 4-fold rotational symmetry (1, 21, 22). Although linker tetramerization is cAMP-dependent, the inter-subunit contacts in the tetramer are mediated by the linker helices A′–D′, which are located more than 20 Å away from the cAMP-binding site in the CBD. The HCN CBD is composed of a contiguous β-subdomain and a noncontiguous α-subdomain (Fig. 1*a*). The β-subdomain forms a β-barrel that contains the phosphate-binding cassette (PBC; Fig. 1*c*), whereas the all-helical α-subdomain includes an N-terminal A-helix, directly connected to the C-linker, and two C-terminal helices critical for HCN activation (Fig. 1, *a* and *c, B* and *C*) (1). In the cAMP-bound structure of HCN, the B–C helices, which are in close proximity to the PBC and cAMP, separate the PBC from the N-terminal helices E′–F′–A, which are collectively referred to as the N3A motif (Fig. 1*c*) (24). This α-subdomain tertiary structure is denoted as the "N3A out/B-C in" topology, where in and out refer to the orientation relative to the PBC and the β-subdomain.

Although the holo-IR structure provides an invaluable picture of the IR in its active state, it is still unclear how the apo-IR causes tonic inhibition of the HCN channel, and how cAMP releases this inhibition. As a first step toward addressing this question, the crystal structure of the tetrameric apo-HCN2 IR was solved, but it was found to be virtually identical to that of the holo-HCN2 IR (r.m.s.d. = 0.5 Å), with the exception of partial uncoiling of the F′-helix and of the C-terminal half of the C-helix, which was unresolved (25). However, it has been suggested that the similarity between the apo- and holo-HCN2 IR tetramer structures might at least in part be due to crystal packing and a co-crystallized bromide ion mimicking the cAMP phosphate (25), as also observed for other apo-CBDs (26, 27). Furthermore, size exclusion chromatography and analytical ultracentrifugation indicate that in solution the IR of HCN2 and HCN4 is primarily monomeric in the apo-form, with minimal or no tetrameric IR detected (11, 21). However, only sparse structural information is currently available on the apo-IR monomer.

Solution FRET data on the monomeric HCN2 IR point to large scale movements in the CBD C terminus upon cAMP binding, resulting in a cAMP-induced disorder to order transition for the distal half of the C-helix coupled to a possible rearrangement of the F′-helix (25). The above studies begin to identify potential alterations in the C-linker and CBD that occur upon cAMP binding to facilitate HCN opening, but it remains still unclear how these alterations actually promote oligomerization of the C-linker and if other conformational or dynamic changes are also required for the cAMP-dependent control of the gating ring that disinhibits channel opening. To address these questions, more information is needed on the changes caused by cAMP binding to the apo-IR HCN monomer.

Herein, we probe by NMR the cAMP-dependent changes in the apo-HCN4 IR monomer in solution. For this purpose, we utilized an HCN4 construct, *i.e.* human HCN4(563–724), that is stabilized in the monomeric state through the deletion of the A′, B′-helices required for tetramerization (11, 13, 21). This HCN4 segment spans the linker helices C′–F′ as well as the CBD and is referred to here as the "extended CBD" or "eCBD" (Fig. 1*b*). The eCBD was analyzed by NMR in the apo-form and bound to either cAMP or the cCMP partial agonist. Surprisingly, our comparative NMR analyses reveal that cAMP binding to the HCN4 eCBD monomer does not significantly affect the C′- and D′-helices of the C-linker, which remain predominantly unstructured when monomeric. However, cAMP drives a drastic change in the remaining eCBD from tetramerization-incompetent to tetramerization-competent structures. The apo-eCBD exists in a pre-equilibrium between these states, in which tetramerization-incompetent conformations prevail. Tetramerization incompetency arises from the orientation of the β-subdomain relative to the E′-, F′-, and A–C-helices observed in the absence of cAMP, which is sterically incompatible with the tight CBD packing required for tetramerization, explaining why the apo-IR is primarily monomeric. Overall, our experiments support a mechanism proposed to rationalize not only why the apo-CBD contributes to the tonic inhibition of the inner gate, but also how cAMP releases this inhibition and facilitates channel opening.

EXPERIMENTAL PROCEDURES

Protein Expression and Purification—HCN4(563–724) and HCN4(579–707) were subcloned into a pET302NT-His vector (Invitrogen) as a rare codon-optimized fusion construct with small ubiquitin-like modifier (SUMO) connected to the N terminus of HCN4 by a tobacco etch virus (TEV) protease-cleavable linker. Both HCN4 constructs were then expressed in the *Escherichia coli* strain BL-21(DE3). Cells were grown in M9 minimal media and induced with 0.5 mM isopropyl β-D-1-thiogalactopyranoside at an optical density of 0.6–0.9 (λ = 600 nm) and further incubated at 18–20 °C for 16 h. After harvesting, the cells were resuspended in the lysis buffer (10 mM HEPES, pH 7.4, with 250 mM KCl and 10% glycerol) and lysed by French press. The cell lysate was centrifuged, and the supernatant was further purified by nickel-nitrilotriacetic acid affinity chromatography with wash buffer (10 mM HEPES, pH 7.4, with 250 mM KCl, 10 mM 2-mercaptoethanol, and 20 mM imidazole) and elution buffer (10 mM HEPES, pH 7.4, with 250 mM KCl, 10 mM 2-mercaptoethanol, and 250 mM imidazole). The His$_6$-small ubiquitin-like modifier (SUMO) was cleaved by His$_6$-tagged tobacco etch virus (TEV) protease prior to a second Ni^{2+} column purification to remove both the cleaved His$_6$-small ubiquitin-like modifier and tobacco etch virus (TEV) protease. The cleaved protein was further purified by gel filtration on a Superdex 75 column.

General NMR Spectroscopy—All NMR spectra were recorded at a temperature of 27 °C, unless otherwise specified, using a Bruker AV 700 spectrometer equipped with a TCI cryo-probe or Bruker AV III 850 MHz Ascend™ spectrometer equipped with a PATXI probe and processed with NMRpipe (28) employing linear prediction, unless otherwise specified, and a resolution enhancing 60° shifted sine squared bell window function. All spectra were analyzed with Sparky (29) using Gaussian line-fitting. Assignments were obtained either through triple-resonance three-dimensional experiments (*i.e.* HNCO, HNCA, HN(CO)CA, CC(CO)NH, H(CCCO)NH, HCCH-TOCSY, CBCA(CO)NH,

and HNCACB) (30) and/or through spectral comparisons if no ambiguities were present. For the triple-resonance data acquisition, uniformly ^{15}N- and ^{13}C-labeled HCN4(579–707) was concentrated to 500 μM in 20 mM MES, pH 6.5, 100 mM KCl, 1 mM DTT, 2 mM EDTA, 2 mM EGTA, 0.02% sodium azide, and 5% ^{2}H$_2$O. The secondary structure probabilities were determined using the secondary chemical shifts via the PECAN software (31). Other specific NMR experiments are discussed below.

Affinity Measurement—Titration of 10 μM HCN4(563–724) with cAMP was performed at 25 °C in 20 mM potassium phosphate buffer, pH 6.5, 50 mM KCl, >99% D$_2$O. Saturation transfer difference (STD) one-dimensional spectra were acquired using a 50-ms spin-lock to minimize interference from protein signals (32). The spectral width was 8389.26 Hz centered at 4.72 ppm. Spectra were digitized with 16 K complex points. The on-resonance saturation frequency was 0.57 ppm, and the off-resonance reference frequency was 30 ppm. The STD amplification factor (STD$_{af}$) was calculated as the product of the STD/STR (saturation transfer reference) ratio for the cAMP ribose H1′ singlet peak at 6.2 ppm, with the ratio of total cAMP and HCN concentrations. STD$_{af}$ values were then normalized with Equation 1,

$$\langle v \rangle = (\text{STD}_{af,[cAMP]} - \text{STD}_{af,[cAMP]=0})$$
$$/(\text{STD}_{af,[cAMP]plateau} - \text{STD}_{af,[cAMP]=0}) \quad \text{(Eq. 1)}$$

with $\langle v \rangle = [PL]/[P]_{Tot}$, where PL is protein-ligand complex, and P is apoprotein. Error bars were determined starting from the spectral noise. Binding isotherms where then fitted using the quadratic equation derived from the dissociation constant equilibrium equation $K_d = [P][L]/[PL]$. The K_d value was determined by minimizing the experimental *versus* calculated $\langle v \rangle$ r.m.s.d.

Chemical Shift Analysis—Uniformly ^{15}N-labeled HCN4(563–724) was concentrated to 100 μM in 20 mM MES, pH 6.5, 100 mM KCl, 1 mM DTT, 2 mM EDTA, 2 mM EGTA, 0.02% sodium azide, and 5% ^{2}H$_2$O. Stock solutions of cCMP (Biolog) and cAMP (Sigma) were prepared using the same buffer as for the protein solution. Starting from the apo samples, stock solutions of the cyclic nucleotide ligands (25 mM) were titrated into the protein solution to full saturation (the final concentrations of ligands were 2.5 mM for cAMP and 5 mM for cCMP). Sensitivity enhanced ^{15}N-^{1}H heteronuclear single quantum coherence (HSQC) spectra with 190 (t_1) and 1024 (t_2) complex points and spectral widths of 31.82 and 14.06 ppm for the ^{15}N and ^{1}H dimensions, respectively, were recorded with 16 scans and a recycle delay of 1.0 s. The ^{1}H and ^{15}N carrier frequencies were set at the water resonance and in the middle of the amide region, respectively. The combined ^{15}N and ^{1}H chemical shifts ($\delta_{1H} + 0.2 \, \delta_{15N}$) from the HSQC spectra of apo and cAMP, cCMP-bound HCN4(563–724) were analyzed using the chemical shift projection analysis, according to previously published protocols (33, 34).

HN-NOE Measurements—HN-NOE data were acquired as reported previously (35, 36) and processed without linear prediction. A 10-s recycle delay was used to include a 5-s proton saturation period. Data were collected in 10 sets of saturated and unsaturated spectra using uniformly ^{15}N-labeled HCN4(563–724) and HCN4(579–707) samples concentrated to 100 μM in 20 mM MES, pH 6.5, 100 mM KCl, 1 mM DTT, 2 mM EDTA, 2 mM EGTA, 0.02% sodium azide, and 5% ^{2}H$_2$O. All spectra were co-added before processing using NMRpipe, resulting in a total 40 scans per serial file for each HN-NOE experiment (with and without ^{1}H saturation). The steady-state HN-NOE values were computed as the ratio of the intensities in saturated to unsaturated spectra. The errors on the HN-NOE values were gauged based on the standard deviation between fit heights in replicate spectra.

H/H Exchange—Amide proton H/H exchange spectra were acquired as described previously (32, 35) using the HCN4(563–724) construct. The protein was concentrated to 100 μM in 20 mM MES, pH 6.5, 100 mM KCl, 1 mM DTT, 2 mM EDTA, 2 mM EGTA, 0.02% sodium azide, and 5% ^{2}H$_2$O. The cAMP-bound sample was prepared by adding 1 mM cAMP in the buffer.

Residual Dipolar Coupling (RDC) Measurements—The residual dipolar couplings were measured in the presence and absence of pf1 (Alsa Biotech) using the sensitivity-enhanced IPAP-type ^{1}H,^{15}N HSQC experiment (37, 38). The spectra were acquired with 128 (t_1) and 1024 (t_2) complex points and spectral widths of 31.82 and 14.06 ppm for the ^{15}N and ^{1}H dimensions, respectively, with eight scans and a recycle delay of 1.0 s. HCN4(579–707) was concentrated to 200 μM in 20 mM MES, pH 6.5, 100 mM KCl, 1 mM EDTA, 1 mM DTT, 0.02% sodium azide, and 5% ^{2}H$_2$O. The anisotropic sample of HCN4(579–707) was prepared with a 6 mg/ml final concentration of pf1 phage.

NOE Measurements—Methyl-Methyl NOEs were measured using a ^{1}H-^{13}C HSQC-NOESY-^{1}H-^{13}C HSQC experiment (39) for ILV methyl selectively [^{1}H,^{13}C]-labeled U-[^{2}H,^{15}N] HCN4(579–707). The protein was expressed in deuterated M9 media, and 1 h prior to induction, 100 mg of methyl-^{13}C-α-ketoisovaleric acid and 100 mg of methyl ^{13}C-α-ketobutyric acid were added to the media. The protein was concentrated to 250 μM in 25 mM phosphate buffer, pH 6.5, 100 mM KCl, 99% ^{2}H$_2$O. The mixing times were 200 and 300 ms. The NOESY-^{15}N HSQC and ^{15}N-HSQC-NOESY-^{15}N HSQC experiments (30) were acquired using uniformly ^{13}C^{15}N-labeled HCN4(579–707). The mixing time was 130 ms. The protein was concentrated to 250 μM in 20 mM MES, pH 6.5, 100 mM KCl, 1 mM EDTA, 1 mM DTT, 0.02% sodium azide, and 5% ^{2}H$_2$O.

Spin Labeling and Paramagnetic Relaxation Enhancement (PRE) Analysis—The spin label 1-oxyl-2,2,5,5-tetramethylpyrroline-3-methyl-methanethiosulfonate (MTSL) was covalently attached to the free cysteine residue in HCN4(579–707). The reducing reagent was exchanged using a PD10 column before the addition of MTSL (35). The reduced HCN4(579–707) was incubated with a 3-fold molar excess of MTSL for 3 h at room temperature. The PREs were quantified through oxidized *versus* reduced rates cross-peak intensities (40) in sensitivity-enhanced ^{1}H^{15}N HSQC spectra with 256 (t_1) and 1024 (t_2) complex points and spectral widths of 31.82 and 14.06 ppm for the ^{15}N and ^{1}H dimensions, respectively. Ninety six scans were recorded with a recycle delay of 1.50 s. After recording the data for the paramagnetic state, 5 mM DTT was added to obtain the diamagnetic control. The diamagnetic sample was incubated at room temperature for 1 h, after which we repeated the same experiments carried out for the paramag-

netic sample (35). HSQC intensity ratios were then calculated as I_{ox}/I_{red}, where I_{ox} is the intensity of signal with MTSL, and I_{red} is the intensity in the reduced sample with DTT.

Structure Calculations by CS-Rosetta (41–52)—The RASREC algorithm from the CS-Rosetta (43, 45) methodology was employed to calculate the structures of HCN4. In addition to chemical shift and residual dipolar couplings, distance restraints were generated from remote homologous structures using the CS-HM protocol (41, 51). Homologous protein structures and their alignment to the target sequence were determined with HHSEARCH (version 2.0.16). The generated alignments spanned residues 588–705, which are nearly the entire modeled region of HCN4. Fragments were picked through the Rosetta3 fragment picker (42, 43) using backbone chemical shifts. From the RASREC pool, which was set to a size of 500, we selected the 10 lowest energy structures as final models. A second calculation was carried out with additional distance restraints derived from methyl-methyl and methyl-HN NOEs in an ILV-labeled sample. Atomic coordinates of apo-HCN4(579–707) have been deposited in the Protein Data Bank with entry code 2MNG.

RESULTS

cAMP Binding to the Monomeric HCN4 eCBD Causes Pervasive Structural Changes in the E′-C-Helices—As a first step in the validation of the HCN4 construct used in our initial NMR studies, *i.e.* the human HCN4(563–724) (eCBD; Fig. 1), we monitored cAMP binding through STD experiments (Fig. 2a). Fig. 2a shows the cAMP-binding isotherm for the HCN4 eCBD, which exhibits a clear dose-response pattern with a well defined plateau, indicative of specific cAMP/eCBD interactions. In addition, nonlinear fitting to a 1:1 binding model resulted in a K_d value in the 1–9 μM range, which is consistent with affinities previously reported for monomeric HCN4 and longer HCN4 constructs at similar concentrations (11, 21). We then acquired HN HSQC spectra of the HCN4 eCBD in the absence of cAMP and in the presence of saturating amounts of cAMP (Fig. 2b) to probe at residue resolution the effect of cAMP binding.

The apo- *versus* holo-HSQC comparison reveals dramatic changes in chemical shifts for the large majority of the eCBD residues (Fig. 2b). A plot of the ppm variations *versus* residue number indicates that cAMP binding has a pervasive effect on the eCBD region from the E′- to the C-helix (Fig. 2c). It is notable that cAMP results in major ppm changes >average not only in the cAMP contact regions, which are nested within the β-subdomain (*i.e.* PBC and the base-binding region), but also in the α-subdomain, including helices that are both N- and C-terminal to the β-subdomain (Fig. 2, c and d). These observations point to the presence of cAMP-dependent structural changes that are not confined only to the B- and C-helices, but extend to the E′–A segment as well, *i.e.* the N3A motif (Fig. 2, c and d). Unlike the N3A, the C′–D′ region, which is part of the HCN IR tetramerization domain (*i.e.* helices A′–D′), displays only relatively minor, below average, chemical shift variations (Fig. 2c). This finding is in agreement with the absence of major changes in self-association upon cAMP binding to the HCN4 eCBD, as expected due to the deletion of the A′, B′ segment required for tetramerization (11, 21, 22). In addition, analytical SEC con-

firms that the HCN4 eCBD remains predominantly monomeric even after cAMP binding (Fig. 1, d and e), as also shown by Chow *et al.* (11). A minor shift toward larger elution volumes is observed upon cAMP binding to the eCBD (Fig. 1e), in agreement with a more compact structure for the cAMP-bound than the apo-eCBD. To further probe the functional relevance of this cAMP-dependent structural change, we have extended our apo *versus* holo comparative NMR analyses to a partial agonist, *i.e.* the cCMP cyclic nucleotide, which results in lower activation efficacies than cAMP (5, 53). Therefore, cCMP is an excellent tool to establish correlations between NMR observables of HCN4 fragments and functionally relevant electrophysiological measurements for full-length integral HCN4 channels.

HCN4 eCBD Exists in a Dynamic Equilibrium of Functionally Relevant Channel Inhibition-competent and -incompetent States—The overlay of the HN-HSQC spectra of hHCN4(563–724) in the absence and presence of saturating concentrations of cAMP or cCMP indicates that several residues far from the ligand contact sites (*i.e.* PBC, base-binding region, and C-helix) exhibit a linear pattern (Fig. 3, a and b). The linearity of this pattern is consistent with the eCBD of HCN4 sampling a dynamic equilibrium between two states that exchange fast in the NMR chemical shift time scale. This means that the observed chemical shifts are linearly weighted averages of the chemical shifts of the two exchanging states and as such they reflect the position of the equilibrium. In this respect, it is notable that the relative order of the peak positions (apo < cCMP < cAMP) appears in agreement with the ranking of the respective $V_{1/2}$ voltages measured through patch clamp electrophysiology for full-length HCN4 channels (53).

To further explore the relationship between the NMR peak positions and the HCN channel efficacies, we computed the distribution of relative fractional activations for cCMP to cAMP based on the NMR chemical shifts (X in Fig. 3, c, d, and g) and we compared the average NMR-based activations to the ligand-induced change in $V_{1/2}$ voltages ($\Delta V_{1/2}$ in Fig. 3h). The X-distribution appears Gaussian and defines an average NMR-based fractional activation for cCMP, which is about half that observed for cAMP (Fig. 3g). This cCMP *versus* cAMP reduction is within error in agreement with the 50% reduction in the $\Delta V_{1/2}$ for cCMP relative to cAMP, measured by electrophysiology of the full-length HCN4 channel (Fig. 3h). These observations suggest that the two states involved in the eCBD dynamic equilibrium sensed by NMR are inhibition-competent and -incompetent, respectively, and that the cyclic nucleotide-dependent modulation of the position of the eCBD equilibrium is a key determinant of HCN channel gating. Hence, we have investigated further the structural changes caused by binding of cAMP to the eCBD.

cAMP Binding to the Monomeric HCN4 eCBD Stabilizes the PBC Helix and Distal Half of the C-helix—To gain further insight into the structural changes caused by cAMP binding to the HCN4 eCBD, we evaluated the secondary structure probabilities based on the secondary chemical shifts in both apo- and holo-forms (Fig. 4, a and b). The secondary structure profile of the cAMP-bound monomeric HCN4 eCBD matches well with
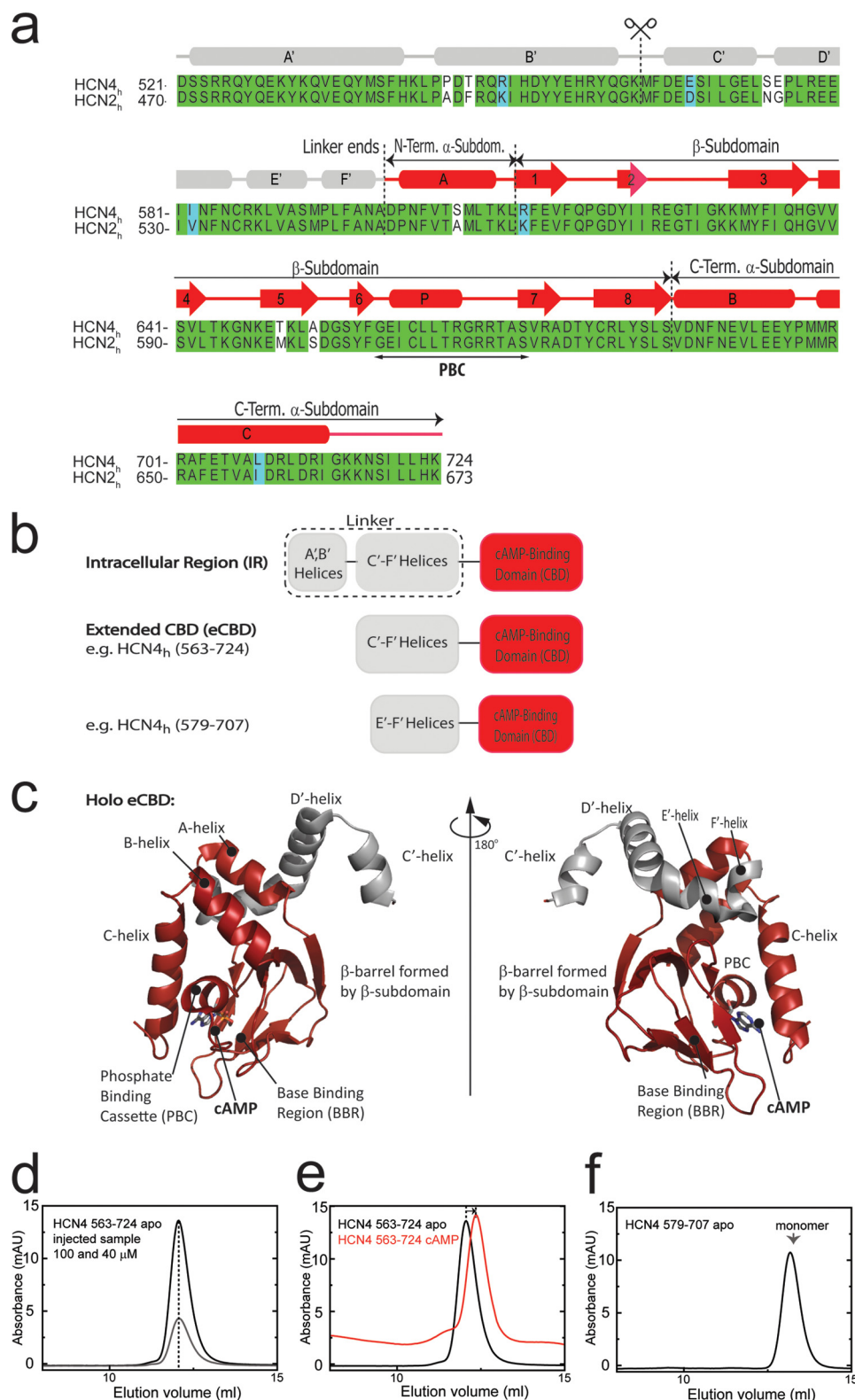
FIGURE 1. **Construct design and architecture of cAMP-bound HCN.** The linker and CBD regions are displayed in *gray* and *red*, respectively. *a,* sequence alignment of the CBDs of human HCN2 and human HCN4. The location of α-helices and β-strands is shown using *red rectangles* and *arrows*, respectively, and was inferred from the crystal structure of cAMP-bound HCN4 (PDB code 3OTF) (22). *b,* domain organization of the intracellular region of HCN4. The human HCN4(563–724) and (579–707) constructs were investigated by NMR. *c,* structure of HCN4(563–724) bound to cAMP (PDB code 3OTF) (22). *d–f,* analytical SEC data of human HCN4. *d,* effect of dilution on apo-HCN4(563–724). Two different concentrations (100 and 40 μM) were injected in the column. *e,* apo *versus* cAMP SEC profiles of HCN4(563–724) injected as a 100 μM solution. *f,* SEC profile of apo-HCN4(579–707) injected as a 100 μM solution. Analytical SEC was preformed with a Superdex 75 10/30 column (GE Healthcare) at 4 °C. Buffer contained 20 mM MES, pH 6.5, 100 mM KCl, 1 mM DTT with or without 1 mM cAMP. *mAU,* milli-absorbance unit.
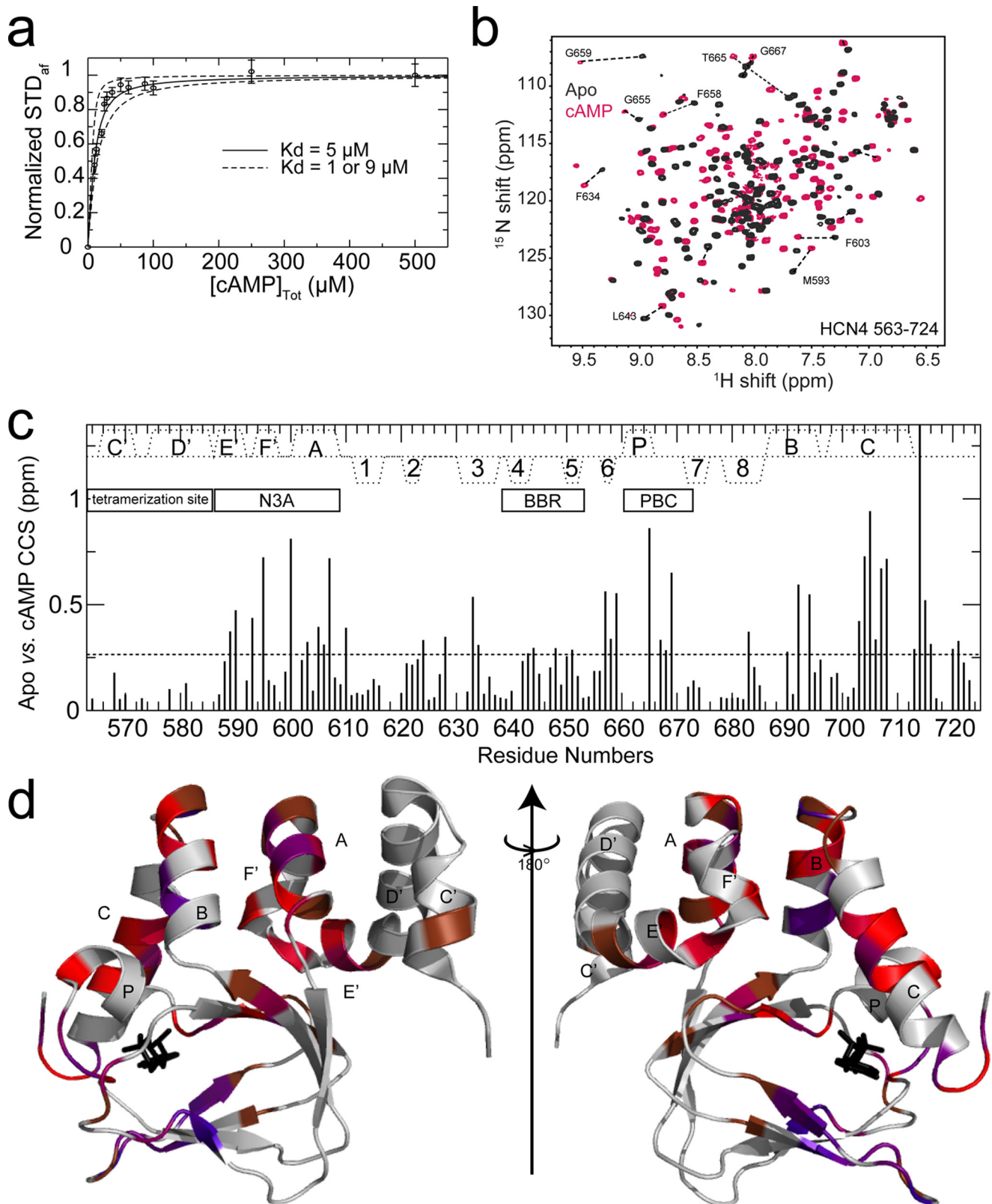
FIGURE 2. **Binding of cAMP to human HCN4(563–724) mapped by STD NMR and chemical shift perturbations.** *a,* binding isotherm for the titration of cAMP into a 10 μM HCN4(563–724) solution monitored through the STD amplification factor (*STD$_{af}$*) normalized to the plateau value and plotted *versus* the total cAMP concentration. The *solid line* represents the binding isotherm corresponding to a K_d value of 5 μM, and the *dashed lines* correspond to K_d values of 1 and 9 μM. *b,* ^{1}H-^{15}N HSQC spectra of 0.1 mM HCN4(563–724) acquired in the absence (*black*) and presence (*red*) of 2.5 mM excess cAMP. Representative peaks are labeled. *c,* compounded ^{1}H,^{15}N chemical shift (*CCS*) differences between apo- and cAMP-bound HCN4(563–724) plotted against the residue number. The secondary structure of cAMP-bound HCN4 is reported as *dotted lines* at the *top* of this panel. *d,* map of apo- *versus* holo-CCS differences onto the structure of cAMP-bound HCN4(563–724) (22). cAMP is shown as *black sticks*. Residue color code: 0.10 ppm $\leq$ CCS $<$ 0.25 ppm is shown in *brown*, 0.25 ppm $\leq$ CCS $<$ 0.50 ppm in *purple,* and 0.50 ppm $\leq$ CCS in *red*.
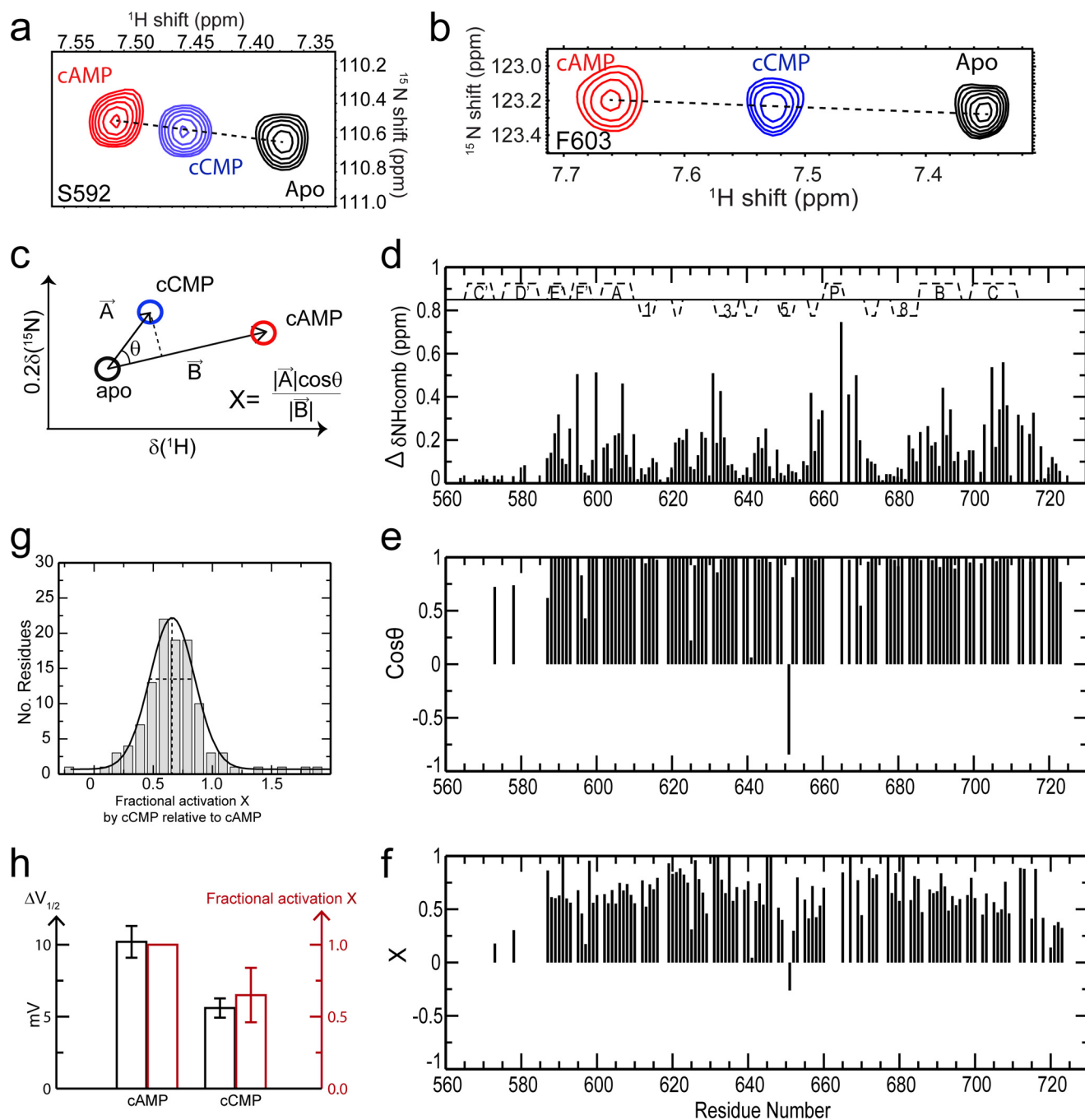
FIGURE 3. **Fractional activation by cCMP partial agonist quantified through the comparative chemical shift analysis of apo *versus* cCMP *versus* cAMP HCN4(563–724).** *a* and *b*, representative HSQC cross-peak for HCN4(563–724) in the apo-form and bound to excess cAMP or cCMP (2.5–5.0 mM). *c*, schematic illustration of the vectors utilized for the projection analysis of NMR chemical shifts. *d*, compounded chemical shift profile of cCMP relative to apo. *e*, cos(θ) residue profile. The angle θ is defined in *c*. *f*, residue-specific fractional shifts (X) toward activation caused by cCMP binding. X is defined in *c*. X was computed only for residues with an apo *versus* cAMP-compounded chemical shift greater than a 0.05 ppm. X values > 1 are off-scale. *g*, distribution of fractional shifts toward activation from *f*, computed using the chemical shift projection analysis (33). The experimental distribution was fitted to a gaussian function. *h*, comparison between the NMR-based average relative % of active state in the cCMP-saturated HCN4(563–724) sample and the $\Delta V_{1/2}$ voltage changes caused by cCMP binding to full-length HCN4 channels measured through electrophysiology (53).

that observed for the E′–C region of the crystal structure solved for holo-tetrameric HCN4 IR (Fig. 4*a*) (21, 22). However, the C′, D′ segment of the IR tetramerization domain does not adopt a clear secondary structure in the monomeric HCN4 (Fig. 4*a*), although it is helical in the tetrameric form (21, 22). The flexibility in the N-terminal region of the HCN eCBD monomer is confirmed by the presence of fast exchanging amides and by a pattern of decreasing HN NOE values detected when moving

from the D′-helix toward the N terminus (Fig. 4*c*). Furthermore, order parameter computations support a disordering of the A′–D′-helices upon tetramer dissociation into monomers (Fig. 4*d*).

The apo-HCN4 eCBD exhibits a secondary structure profile that is remarkably similar to that of the holo-form but for two notable exceptions, the PBC and the distal half of the C-helix (Fig. 4*b*). In the absence of cAMP, the PBC helix between β6
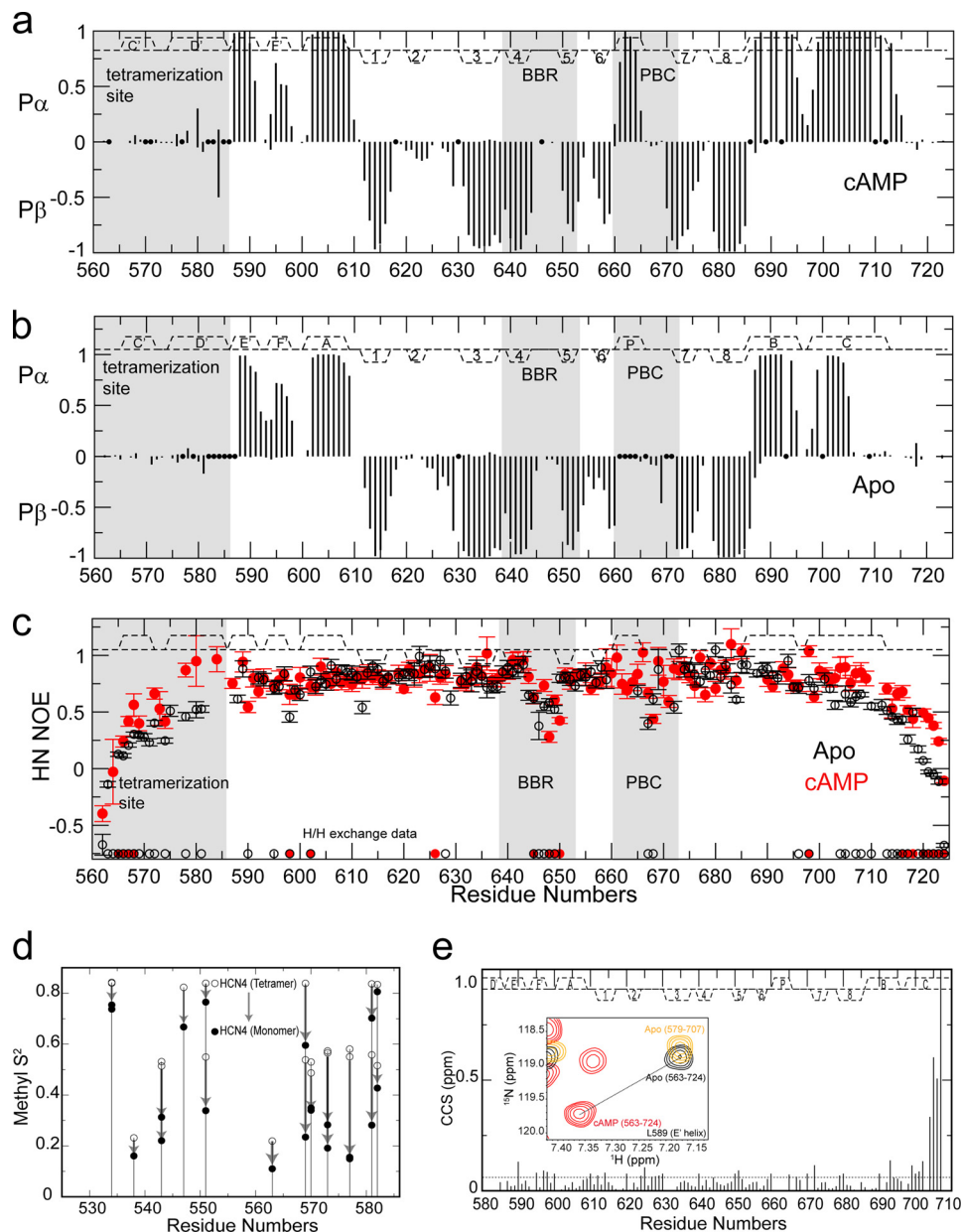
FIGURE 4. **Secondary structure and picosecond-nanosecond dynamic profile of apo- and cAMP-bound human HCN4(563–724).** NMR chemical shift-based secondary structure of HCN4(563–724) in the presence of excess cAMP (*a*) and in the apo-form (*b*). Helical and strand probabilities are reported as positive and negative values, respectively. *a* and *b*, residues for which HN assignments are not available are flagged with a *dot*. *c*, HN-NOE *versus* residue plot for HCN4(563–724) in the presence of excess cAMP (*red*) and in the apo-form (*black*). The *circles* at the bottom of *c* denote the presence of fast H/H exchange as indicated by the observation of CLEANEX cross-peaks in the apo-form (*empty circles*) and in the presence of excess cAMP (*red filled circles*). *d*, changes in methyl order parameters (S^2) for the region-spanning helices A'–D' as computed based on the HCN4 structure (chain A of PDB code 3OTF) either as an isolated monomer (*filled circles*) or assembled as a tetramer (*open circles*). Computations were executed through the "S2" software (81). These computations do not consider the possible unfolding of the A'–D'-helices upon tetramer dissociation, and therefore it is possible that the experimental order parameters for the monomer are lower than those computed here. *e*, CCS differences between apo-human HCN4(579–707) and apo-human HCN4(563–724). *Dashed lines* outline the secondary structure as per the PDB code 3OTF (22).

and β7 is not observed (Fig. 4*b*). Although some PBC residues could not be assigned due to line broadening indicative of millisecond to microsecond dynamics, the lack of significant helical probabilities in the apo-PBC is consistent with a destabilization of the PBC helix, which is clearly observed in the holo-eCBD (Fig. 4*a*). The destabilization of the apo-PBC is also supported by the observation of fast exchanging amides (Fig. 4*c*). The other major change in secondary structure caused by cAMP is in the C-helix region spanning residues 705–715, which is unstructured in the absence of cAMP

(Fig. 4*b*) but becomes structured in the presence of cAMP (Fig. 4*a*). The cAMP-induced structuring of this segment is independently supported by a consistent increase in the HN NOE values upon cAMP binding and by the cAMP-induced protection of several C-helix amides that are fast exchanging in the apo-form (Fig. 4*c*). Interestingly, no major changes in secondary structure are observed for the rest of the α-subdomain (Fig. 4, *a* and *b*), suggesting that the marked cAMP-dependent HN chemical shift variations observed for helices E'–B (Fig. 2, *c* and *d*) arise primarily from changes in tertiary
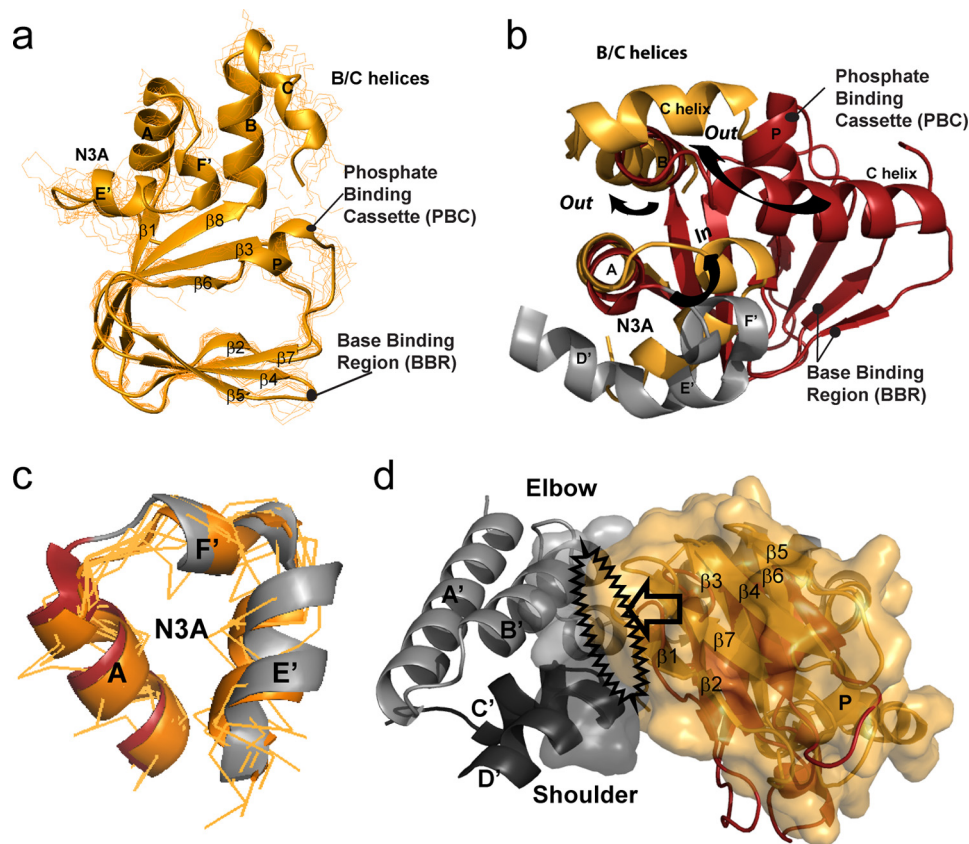
FIGURE 5. **Proposed structural model for apo-human HCN4(579–707).** *a,* overlay of 10 representative structures of apo-HCN4(579–707) as refined through CS-Rosetta. The ribbon represents the average structure of the ensemble. *b,* apo (average, *orange*) *versus* cAMP-bound (*gray* and *red*) CBD comparison. The holo-HCN4 structure was obtained from the PDB code 3OTF (22). Upon cAMP removal, the A-helix rotates around its axis and slightly tilts thus moving the N3A motif closer to the PBC and the β-barrel (N3A in orientation). Unlike the N3A region, the B/C-helices move away from the PBC upon removal of cAMP (B/C out orientation). *c,* apo (*orange*) *versus* holo-N3A overlay, revealing that the cAMP-dependent N3A movement occurs in first approximation as a rigid-body, *i.e.* the average relative orientation of the helices within the N3A motif does not change significantly upon cAMP binding. The ribbon represents the average structure of the ensemble, similarly to *a*. *d,* "hybrid" HCN4 hypothetical model arising from the overlay of the N3A motifs from the active-state IR region (*i.e.* A'-β segment from the A protomer of the PDB structure 3OTF; linker is in *light gray* and CBD component is in *red*) and from the inactive state average structure (*i.e.* E'-β segment of apo-HCN4(579–707) shown in *orange*). Helices C'–D' from an adjacent protomer are shown in *dark gray* to illustrate the elbow-shoulder inter-molecular contacts that stabilize the tetramer. Surfaces are shown for the IR tetramerization domain residues that in the holo-tetramer are in contact with the β-subdomain, and for the apo-HCN4 structure. The *arrow* and *black jagged oval* highlight the site of steric clashes between the apo β-barrel and the IR tetramerization domain, as quantified in Table 2.

structure. This type of helical re-orientations is best probed through RDCs, which are highly sensitive to both hinge and on-axis rotations of helices (54, 55). To facilitate the measurement of RDCs, we reduced the overlap in the helical spectral regions, which are typically less dispersed than β-sheets, by deleting the N- and C-terminal disordered residues (*i.e.* 563–578 and 708–724). These segments are to a large extent unstructured in the apo-eCBD as shown by both the secondary chemical shifts and the decreased HN NOE values (Fig. 4, *b* and *c*). Hence, removal of these regions is not expected to significantly perturb the rest of the apo-HCN4 eCBD. This prediction is supported by the overall minimal chemical shift differences observed between the apo(563–724) and the apo (579–707) HCN4 constructs (Fig. 4e). Furthermore, the analytical SEC elution profile confirms that apo-HCN4(579–707) remains monomeric (Fig. 1f). Thus, this construct is ideal for further NMR studies on the structure adopted by the apo-eCBD monomer.

cAMP Binding Causes a Shift in the α-Subdomain Tertiary Structure from an "N3A in/B–C out" to an "N3A Out/B-C In" Topology—A 10-structure model of apo-HCN4(579–707) was built (Fig. 5a and Table 1) by CS-Rosetta using chemical shifts,

TABLE 1

**Structural statistics of Apo HCN4 (579–707)**

Residues	131[a]
Restraints	
Evolutionary restraints	4502
Total HN RDCs	115
Residues with good[b] TALOS$^+$ prediction	94
Average r.m.s.d. to mean structure (Å)	
Backbone atoms (CING)	0.90 ± 0.19
Heavy atoms (CING)	1.43 ± 0.16
Ramachandran statistics (CING)	
Residues in most favored regions	89.6%
Residues in allowed regions	10.4%
Residues in generously allowed regions	0.0%
Residue in disallowed regions	0.0%

[a] 129 residues for HCN4(579–707) and two additional residues from the restriction site (Asn and Ser).
[b] "Good" TALOS$^+$ predictions are defined as in Ref. 82.

homology restraints, and RDCs (Fig. 6a) (41–52). Overall, the model is well converged, as supported by local r.m.s.d. values below 0.2 Å for most residues (Fig. 6b). Selected regions exhibit r.m.s.d. >0.2 Å, including the N and C termini, the F'–helix, the $\beta2$–3 and $\beta4$–5 loops as well as the PBC (Fig. 6b). These local r.m.s.d. maxima match well with local minima in the HN NOE profile of apo-HCN4(579–707) (*orange plot* in Fig.
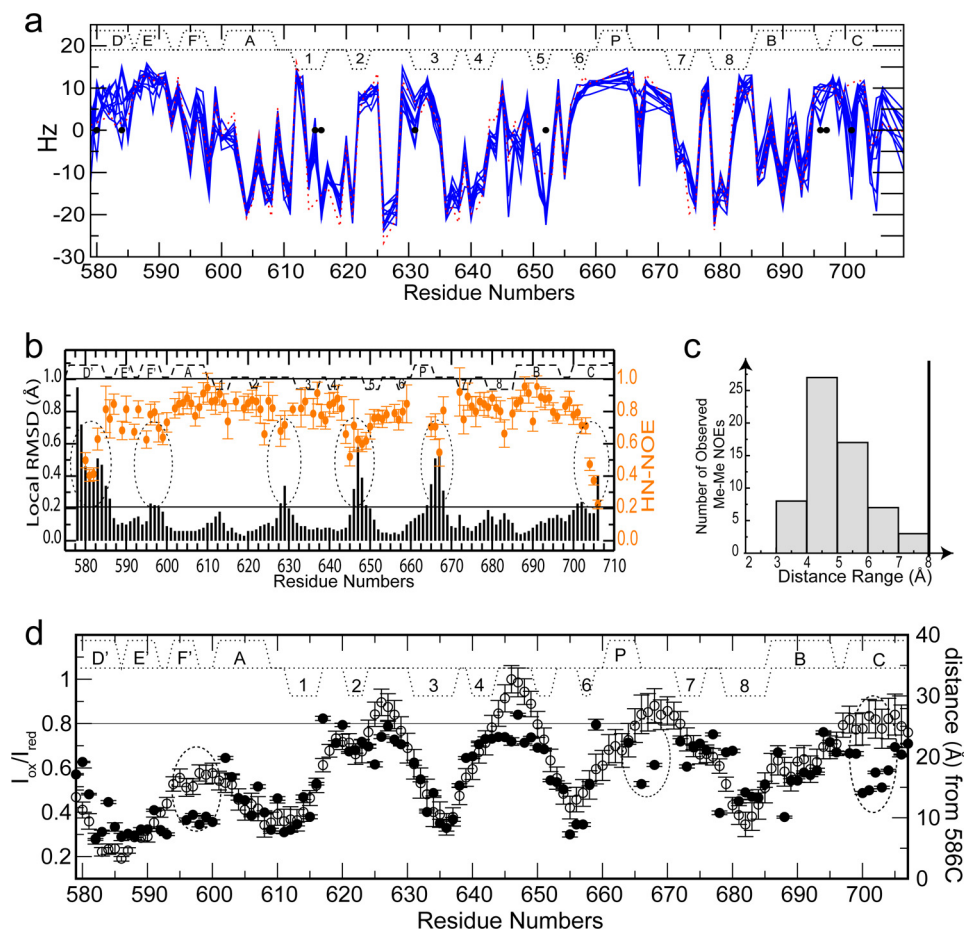
FIGURE 6. **Validation of the structural model for apo-human HCN4(579–707).** *a,* experimental *versus* back-calculated RDC comparison for apo-human HCN4(579–707). The experimental backbone amide RDCs (*red dotted line*) show overall good agreement with the back-calculated RDCs (*blue lines*). *Black dots* represent residues for which cross-peaks were overlapping in the HSQC spectra. *b,* comparative analysis of the residue-specific local r.m.s.d. and HN-NOE profiles of apo-human HCN4(579–707). The *dotted ovals* highlight regions corresponding to local maxima and local minima in the r.m.s.d. and HN-NOE values, respectively. The secondary structure is reported as *dashed lines*. The local r.m.s.d. was computed using the structure bundle shown in Fig. 5*a*. *c,* distance distribution for the Me-Me NOEs measured for apo-HCN4(579–707). Histogram showing the number of observed NOEs in apo-HCN4(579–707) for different distance ranges. Methyl-methyl distances have been calculated between methyl carbon atoms. All the observed NOEs correspond to distances less than 8 Å. *d,* PRE profile for apo-human HCN4(579–707) spin-labeled at Cys-586. The PREs were quantified in terms of relative HSQC intensity attenuations (I_{ox}/I_{red}; *filled circles*) and were compared with the average amide distances from the sulfur atom of Cys-586 computed based on the apo-human HCN4(579–707) structures (*open circles*). The I_{ox}/I_{red} ratios <0.8 are expected to correlate linearly with distances, unless internal dynamics is present. Significant contributions from spin labels at other Cys sites (*i.e.* Cys-662 and Cys-679) were ruled out as follows. Cys-679 is well structured (HN-NOE ≥0.8 and its side chain is inaccessible to solvent: the solvent-accessible surface area in the apo-structure is 0 Å^2). For Cys-662, the corresponding side chain solvent-accessible surface area is 1 Å^2 and, although the HN NOE value for this residue is not available, the profile of amide distances from Cys-662 does not match the experimental intensity data. The *dotted ovals* indicate local deviations between the PRE ratios and the distances calculated based on the structures, possibly arising from the presence of structural dynamics.

6*b, dotted ovals*), suggesting that the increased r.m.s.d. values observed in these segments reflect genuinely enhanced picosecond-nanosecond local dynamics rather than simply a lack of experimental restraints.

To further validate the structural model of apo-HCN4(579–707) built by CS-Rosetta based on chemical shifts, evolutionary restraints, and RDCs, we measured methyl-methyl NOEs in an ILV-methyl protonated but otherwise deuterated sample of apo-HCN4(579–707) (Fig. 6*c*). Because of the extensive degree of deuteration, both spin diffusion and transverse relaxation are reduced relative to fully protonated samples. This allows the measurement of NOEs for long range distances (≤8 Å), which are sensitive to tertiary structure changes, such as those occurring in the HCN4 eCBD upon cAMP binding. As shown in Fig. 6*c*, the CS-Rosetta structures are in agreement with the experimental methyl-methyl NOEs, although the latter were not

used as restraints in the structural refinement. Further CS-Rosetta iterations, with Me-Me and NH-involving NOEs explicitly included as restraints did not result in increased convergence nor in different models. In addition, the CS-Rosetta structures are supported by PRE measurements for an apo-HCN4(579–707) sample in which a spin label was covalently linked to the endogenous Cys-586 (Fig. 6*d*). PRE values quantified as oxidized *versus* reduced intensity ratios (I_{ox}/I_{red}) are expected to vary linearly with distances when less than ~0.8 (40) and should exhibit a trend similar to that of the amide distances from Cys-586 predicted from the CS-Rosetta model. The PRE *versus* distance linearity is apparent in Fig. 6*d*, except for regions experiencing enhanced dynamics and greater flexibility, such as the F′-helix, the PBC, and the C terminus (Fig. 6, *b* and *d*). The local flexibility in these regions contributes to the localized deviations from the linear I_{ox}/I_{red} *versus* distance trend. We conclude

TABLE 2

Potential energies of steric contact among structural elements of the active state and "hybrid" tetramer structures of HCN4

Structure	αA′-αB′/β-core intra-monomer contact energy[a] (kcal/mol)		αC′-αD′/β-core inter-monomer contact energy[a] (kcal/mol)		Total IR tetramerization domain/β-core[a] contact energy (kcal/mol)	
	αA overlay[b]	N3A overlay[b]	αA overlay[b]	N3A overlay[b]	αA overlay[b]	N3A overlay[b]
NMR 1	$\sim 10^1$	$\sim 10^3$	$\sim 10^2$	-6.12	$\sim 10^2$	$\sim 10^3$
NMR 2	$\sim 10^9$	$> 10^9$	$\sim 10^6$	$\sim 10^3$	$\sim 10^9$	$> 10^9$
NMR 3	$\sim 10^6$	$\sim 10^9$	$> 10^9$	$\sim 10^5$	$> 10^9$	$\sim 10^9$
NMR 4	$\sim 10^8$	$\sim 10^7$	$\sim 10^4$	$\sim 10^3$	$\sim 10^8$	$\sim 10^7$
NMR 5	$\sim 10^8$	$> 10^9$	$\sim 10^9$	$\sim 10^2$	$\sim 10^9$	$> 10^9$
NMR 6	-7.49	-1.93	$\sim 10^7$	$-2.13\ (\sim 10^7)^c$	$\sim 10^7$	$-4.06\ (\sim 10^7)^c$
NMR 7	$> 10^9$	$> 10^9$	$> 10^9$	$\sim 10^8$	$> 10^9$	$> 10^9$
NMR 8	$> 10^9$	$> 10^9$	-7.01	$\sim 10^3$	$> 10^9$	$> 10^9$
NMR 9	$\sim 10^3$	$\sim 10^9$	$\sim 10^9$	-12.05	$\sim 10^9$	$\sim 10^9$
NMR 10	$\sim 10^4$	$> 10^9$	$\sim 10^4$	$\sim 10^4$	$\sim 10^4$	$> 10^9$
NMR median average	$\sim 10^8$	$\sim 10^9$	$\sim 10^7$	$\sim 10^3$	$\sim 10^9$	$\sim 10^9$
Active state tetramer[d]	-16.83		-11.84		-28.67	

[a] The energies of steric contact between structural elements X and Y were computed from the van der Waals (VDW) energies using NAMD as follows: contact E (X versus Y) = VDW (X and Y together) − VDW (X alone) − VDW (Y alone). The CHARMM 27 force field was used to calculate the van der Waals energies.

[b] For each NMR-derived "hybrid" tetramer, energy values for two structures are listed in each row as follows: a structure consisting of the αA′–αF′ segment of the active state structure (PDB code 3OTF), and the αA–αC segment of the respective NMR structure, grafted together via αA helix backbone overlay (first value); and a structure consisting of the αA′–αD′ segment of the active state structure (PDB code 3OTF), and the αE′–αC segment of the respective NMR structure, grafted together via αE′–αA region (N3A) backbone overlay (second value).

[c] The number in parentheses is the contact energy arising from the inter-molecular αB/C versus β-core clash.

[d] Tetramer derived from structure 3OTF obtained from the RCSB Protein Data Bank.

that the CS-Rosetta structures of the apo-HCN4(579–707) are supported not only by the measured chemical shifts and RDC values, but also by independent NOE and PRE measurements.

The structures of the apo-HCN4 eCBD reveal several critical differences relative to its holo-form (Fig. 5*b*). In apo-HCN4 the axis of the B-helix is tilted away from the PBC through a hinge rotation that moves the C-helix outward relative to the cAMP-binding site in the β-subdomain (*i.e.* "B-C out" arrangement, Fig. 5*b*). The movement of the C-helix away from the β-subdomain allows the E′- and F′-helices to move closer to the PBC (*i.e.* "N3A in" arrangement, Fig. 5*b*) primarily through a rotation of the A-helix around its axis. Hence, the α-subdomain tertiary structure topologies in apo -and holo-HCN4 are reversed. The eCBD α-subdomain topology is "N3A in/B-C out" before cAMP binding but switches to "N3A out/B-C in" after. This switch in α-subdomain topology does not significantly alter the orientation of the N3A helices E′–F′-A relative to each other (Fig. 5*c*) but changes the orientation of the β-subdomain relative to the N3A motif (Fig. 5, *b* and *d*).

To explore how the cAMP-dependent β-subdomain/N3A reorientation affects the packing of the CBD within the tetramer, and in turn the propensity of the HCN4 IR to tetramerize, we superimposed the N3A motif of the apo-HCN4 structure solved here to the N3A region of the holo-HCN4 tetramer (PDB code 3OTF) (22) and analyzed how the packing of the β-subdomain is affected by the absence of cAMP (Fig. 5*d*). In the presence of cAMP, the β1–2 turn of the β-subdomain is in close contact with a surface defined by two contiguous helices, helix B′ from the same protomer as the β-subdomain and helix D′ from an adjacent protomer in the tetramer (Fig. 5*d*). The B′- and D′-helices are respective parts of the "elbow" and "shoulder" contacts that stabilize the tetramer. In the absence of cAMP, the β-subdomain moves toward the IR tetramerization domain, resulting in steric clashes between the β-barrel and the B′/D′ elbow/shoulder surface (Fig. 5*d*). The steric hindrance with the B′/D′-helices leads to a marked surge in van der Waals interaction energies, as sum-

marized in Table 2, and hence to a destabilization of the tetramer. Overall, the apo-HCN4 eCBD structure is not compatible with the tight packing imposed by tetramerization of the HCN IR. Upon cAMP binding, the β-subdomain reorients removing the steric clashes with the IR tetramerization domain, thereby stabilizing the tetramer and explaining why cAMP causes a transition from tetramerization-incompetent to tetramerization-competent states.

DISCUSSION

A Model of HCN Auto-inhibition and cAMP-dependent Activation—Our data support a model for the IR of HCN4 in which the C-linker region spanning the IR tetramerization domain, *i.e.* helices A′–D′, remains intrinsically unstructured or only partially structured when the IR is monomeric (Fig. 7, *a–d*), whereas the rest of the IR, including the CBD, exists in a dynamic equilibrium between auto-inhibited and active states (Fig. 7, *a* and *b*). In both states, the internal structures of the N3A and β-barrel remain largely conserved, but they are oriented differently in relation to each other. In the auto-inhibited state, the N3A motif is in close proximity to the β-barrel (N3A in, Fig. 7*a*) because of an outward movement of the C-terminal B–C-helices (B/C out, Fig. 7*a*), which would otherwise clash with the N3A in arrangement. In the active state, the CBD switches to a swapped topology, where the N3A adopts an "out" orientation distal from the β-subdomain because the B/C-helices are tilted in an "in" arrangement (Fig. 7*b*). In the absence of cAMP, the auto-inhibited *versus* active equilibrium is shifted toward the former state, whereas the latter has greater affinity for cAMP and is therefore favored when the cyclic nucleotide is available to bind.

A key determinant of the selectivity of cAMP for the active state is its ability to stabilize the C-terminal half of the C-helix, which serves as a lid for capping the adenine base (Fig. 7*c*) (1, 3, 56). The active *versus* inactive selectivity of cAMP results in the coupling between the cAMP binding and the conformational equilibria of the eCBD, which is described by the allosteric thermodynamic cycle depicted in Fig. 7, *a–d*. In all four states of the
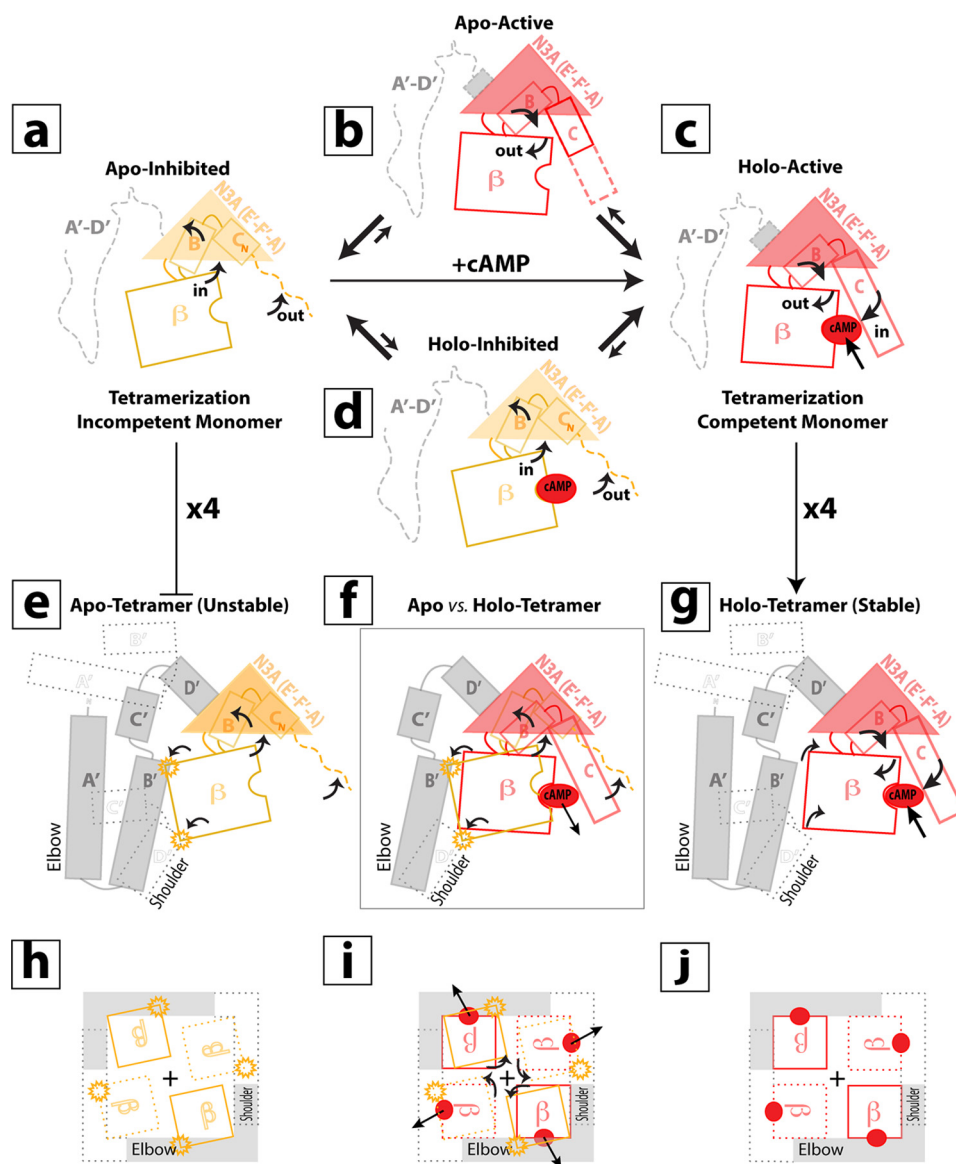
FIGURE 7. **Proposed model for auto-inhibition of HCN4 by the IR, spanning the IR tetramerization domain (*i.e.* helices A′–D′), shown in *gray*, the N3A and the remaining part of the CBD, both shown in either *orange* (Inhibited) or *red* (Active).** The N3A motif (*triangle*) is composed of helices E′–F′–A, which are N-terminal to the β-subdomain of the CBD. The CBD includes also helices B–C, which are C-terminal to the β-subdomain and function as a lid for cAMP. The N3A orientation is kept constant in all the panels. *Dashed lines* denote unfolded or partially unfolded segments. *a–d,* four-state thermodynamic cycle for the cAMP-dependent allostery of the monomeric HCN4 IR, resulting from the coupling of the cAMP-binding equilibrium (*i.e.* apo *versus* holo) and the conformational change equilibrium (*i.e.* inhibited *versus* active). *e* and *f,* models for the tetrameric HCN4 IR. *Dotted lines* indicate helices from distinct but adjacent protomers within the tetramer. Tetramerization promotes folding of helices A′–D′. However, the apo-tetramer is unstable due to steric clashes between the β-subdomain and the IR tetramerization domain, which are highlighted as *yellow suns*. The allosteric conformational transition driven by cAMP binding changes the relative orientation of the N3A and β-subdomain, eliminating the steric clashes that destabilize the apo-tetramer, as shown in *g*. *f* illustrates the apo-tetramer *versus* holo-tetramer comparison. *h* and *j,* schemes of the apo (*h*), holo (*j*), and apo *versus* holo (*i*) HCN4 intracellular region tetramer viewed parallel to the 4-fold axis, denoted by the + sign in the center of each tetramer. Similarly to *e–g*, *yellow suns* indicate steric clashes, and *red filled ovals* represent cAMP molecules.

cycle for the monomeric IR, the C-linker region spanning the IR tetramerization domain remains largely unstructured, regardless of cAMP availability or the position of the auto-inhibitory equilibrium (Fig. 7, *a–d*).

The four helices of the C-linker composing the IR tetramerization domain, *i.e.* A′–D′, are stabilized upon tetramer formation by "elbow-shoulder" swapped contacts between the A′–B′ motif of one protomer and the C′–D′-helices of the adjacent subunit (Fig. 7, *e–g*) (1, 21, 22). The stabilized D′-helix in the tetramer recruits and orients the contiguous N3A motif with respect to the IR tetramerization domain (1, 21, 22, 25). How-

ever, in the absence of cAMP, the N3A in/B-C out tertiary structure of the apo-eCBD leads to a steric clash between the β-subdomain and the elbow-shoulder surface defined by helix B′ of the same protomer and helix D′ of the adjacent protomer (Fig. 7, *e* and *h*), making an apo-tetramer unstable. By switching the N3A in/B-C out to the N3A out/B-C in conformation, cAMP binding effectively removes the steric hindrance that destabilizes the apo-tetramer (Fig. 7, *f* and *i*), resulting in a stable holo-tetramer (Fig. 7, *g* and *j*). This simple model (Fig. 7) explains why apo monomeric IR is tetramerization-incompetent (Fig. 7, *a*, *e*, and *h*) and why tetramerization competence is
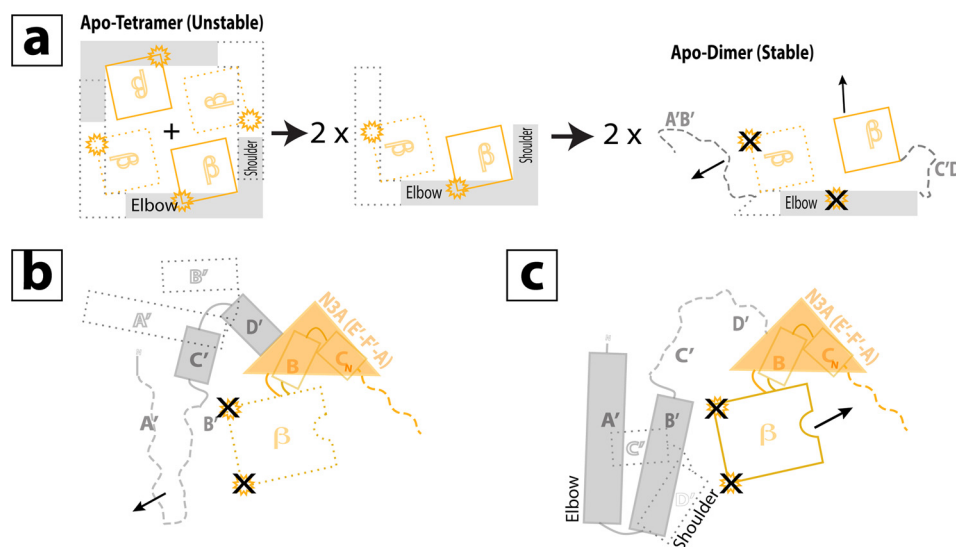
FIGURE 8. **Proposed models for apo-HCN dimer of dimers.** Scheme illustrating why in the apo-HCN dimer the eCBD does not necessarily lead to steric clashes, unlike in the apo-tetramer (Fig. 7, *e* and *h*). The color codes are as in Fig. 7. As in Fig. 7, *dashed lines* denote regions that are only partially structured or unstructured, and *dotted rectangles* indicate helices belonging to an adjacent protomer. *a*, stepwise dissociation of the unstable apo-tetramer into dimers, in which the structuring effect of self-association is preserved for only a single elbow-shoulder interface per dimer. The increased linker flexibility in the dimer relative to the tetramer allows the β-subdomain of the CBD to move and relax the steric clashes (*suns* with "*X*"), as shown in panels *b* and *c*, which correspond to the two different protomers within the dimer.

restored by cAMP (Fig. 7, *c*, *g*, and *j*). Because tetramerization of the HCN2 and HCN4 IR in solution appears to reflect a process promoted by cAMP in the full-length channel (1, 11, 21, 57), we propose that the scheme in Fig. 7 represents one of the possible molecular mechanisms for auto-inhibition of opening by the IR and its relaxation by cAMP in the full-length HCN channel.

The proposed mechanism (Fig. 7) explains several other previously reported observations on the activation of HCN truncation mutants (23). For example, the scheme of Fig. 7 rationalizes why deletion of the C-terminal C-helix results in an HCN2 channel that remains auto-inhibited both in the absence and presence of cAMP (23). The C-helix truncation does not affect significantly the apo-form, where the C-helix is already partially unstructured and in an out orientation (Fig. 7*a*). However, the C-helix deletion removes the lid for cAMP and thus the N3A in/B-C out to N3A out/B-C in conformational switch does not take place when cAMP binds. Furthermore, the mechanism of Fig. 7 explains why the deletion of the whole CBD activates the HCN channels, mimicking the action of cAMP binding to the wild-type HCN (23). In the absence of the CBD, the steric clashes that destabilize the apo-tetramer (Fig. 7, *e* and *h*) are effectively eliminated, allowing tetramerization, and presumably facilitation of opening in the full-length channel, to occur even in the absence of cAMP.

The model of Fig. 7 is also supported by other independent observations. For instance, the structure of the HCN2 IR solved in the absence of cAMP reveals a tetramer in which both the N3A and the β-barrel preserve the same orientation relative to the IR tetramerization domain (TD) as observed in the cAMP-bound tetramer (25). This observation has two key implications. The first is that, as posited in the proposed model (Fig. 7, *e–j*), the positioning of the N3A motif relative to the TD is dictated primarily by the tetramerization, rather than by cAMP availability. The second is that, once the N3A is positioned relative to the TD, the in orientation of the β-barrel is incompatible with the tetramer and, if the

tetramer is imposed through the use of high concentrations, as in the case of crystallization, the β-barrel is forced to shift to the out orientation to relieve the steric clashes with the TD and fit in the tightly packed tetramer, as observed (1, 25).

The tetramerization-induced shift of the eCBD from the N3A in/B-C out to the N3A out/B-C in state, which exhibits higher affinity for cAMP, is also independently confirmed by experiments showing that the tetrameric forms of the HCN2 and HCN4 IR bind cAMP with affinities significantly higher than those measured for the monomeric IR (11). Therefore, cAMP binding and tetramerization appear mutually coupled and an enhancement in one promotes the other. This mutual coupling may explain the differences in cAMP sensitivities observed for different HCN isoforms (21). Overall, the currently available data support the mutual exclusivity between the apo-eCBD N3A in/B-C out topology and the formation of a tightly packed HCN tetramer. Nevertheless, it should be noted that the apo-eCBD N3A in/B-C out structure might be compatible with oligomeric forms of the IR other than tetramers.

The model of Fig. 7 is consistent with the presence of dimers (Fig. 8). This is because not only apo-monomers but also apo-dimers may release the steric hindrance identified in the apo-tetramer (Fig. 7, *e* and *h*) due to the intrinsic flexibility of the A′–D′ region (Fig. 7*a*). In the scheme of Fig. 7, *e* and *h*, the presence of steric clashes between the β-subdomain and the B′/D′ elbow/shoulder surface of the TD requires the simultaneous structuring through self-association of both the A′B′ and the C′D′-helical pairs belonging to the same protomer as the β-barrel causing the hindrance. If either one of these A′B′ or C′D′ pairs is not fully structured, then the orientation of the N3A motif relative to the TD is not fully defined, given the intrinsic dynamics observed for the TD region in the absence of self-association (Fig. 8*a*). The steric clashes generated by the β-subdomain can then be effectively reduced by a rigid-body movement of the N3A and

β-subdomain away from the TD, without the need of a N3A in/B-C out to N3A out/B-C in shift of the eCBD. This is the case for HCN dimers (Fig. 8), in which the C′D′ of one protomer is not stabilized by the A′B′ of an adjacent protomer or vice versa. Hence, in the dimer, unlike in the tetramer, the A′B′ and C′D′ pairs cannot both be simultaneously stabilized though self-association, and thus steric hindrance is released even without cAMP (Fig. 8). We conclude that the model of Fig. 7 is fully consistent with the apo-HCN IR existing not only as a monomer but also as a dimer of dimers (Fig. 8), as proposed previously based on electrophysiological measurements (57, 58).

Our data also suggest a possible mechanism for the action of cCMP, which has been shown to act as a partial agonist using electrophysiological methods (1, 53). Partial agonism could arise either from a different conformational change occurring in response to the partial agonist or from a structural change that is similar to the alteration produced by the endogenous allosteric effector, but it corresponds to a reduced shift in the position of the auto-inhibitory equilibrium (59). Our results support the second hypothesis, whereby cCMP exhibits a lower tetramerization-competent *versus* tetramerization-incompetent state selectivity than cAMP. Consequently, the tetramerization-competent state is more stable when bound to cAMP than cCMP, resulting in a reduced equilibrium shift upon cCMP binding to the CBD.

Last but not least, the model of Fig. 7 reveals that the HCN eCBD exhibits similarities with the allosteric conformational switch previously observed for PKA (60–69) and distinct differences from EPAC, which is another pivotal eukaryotic cAMP receptor with a structurally homologous α/β-CBD (70–75). In the EPAC CBD, the cAMP-dependent structural changes are mainly confined to the helix C-terminal to the β-subdomain (34). Upon cAMP binding, this helix tilts toward the PBC and during the hinge rotation the helix partially unfolds, unlike what was observed in HCN. In addition, unlike HCN, in EPAC no major cAMP-dependent rearrangements are observed for the N3A motif, whereas a clear N3A in/B-C out to N3A out/B-C in shift was reported for both CBDs of the regulatory subunit of PKA (24, 60–75), similarly to bacterial CNG channels (76). In this respect, the HCN CBD resembles more closely that of PKA rather than that of EPAC. However, it is likely that differences may still exist between the CBDs of PKA and HCN. For instance, for one of the PKA CBDs, the apo pre-equilibrium does not appear to be as highly skewed toward the inactive state as in the CBD of the apo-HCN IR (35), explaining why the regulatory subunit of PKA, unlike HCN (11), binds cAMP with a low approximate nanomolar affinity. The differences in binding and allosteric properties among different eukaryotic CBDs will facilitate the selective targeting of CBDs as required for therapeutic purposes (77–80).

REFERENCES

1. Zagotta, W. N., Olivier, N. B., Black, K. D., Young, E. C., Olson, R., and Gouaux, E. (2003) Structural basis for modulation and agonist specificity of HCN pacemaker channels. *Nature* **425,** 200–205
2. Robinson, R. B., and Siegelbaum, S. A. (2003) Hyperpolarization-activated cation currents: from molecules to physiological function. *Annu. Rev. Physiol.* **65,** 453–480
3. Trudeau, M. C., and Zagotta, W. N. (2003) Calcium/calmodulin modulation of olfactory and rod cyclic nucleotide-gated ion channels. *J. Biol. Chem.* **278,** 18705–18708
4. Kaupp, U. B., and Seifert, R. (2002) Cyclic nucleotide-gated ion channels. *Physiol. Rev.* **82,** 769–824
5. DiFrancesco, D., and Tortora, P. (1991) Direct activation of cardiac pacemaker channels by intracellular cyclic AMP. *Nature* **351,** 145–147
6. Kusch, J., Thon, S., Schulz, E., Biskup, C., Nache, V., Zimmer, T., Seifert, R., Schwede, F., and Benndorf, K. (2012) How subunits cooperate in cAMP-induced activation of homotetrameric HCN2 channels. *Nat. Chem. Biol.* **8,** 162–169
7. Zagotta, W. N., and Siegelbaum, S. A. (1996) Structure and function of cyclic nucleotide-gated channels. *Annu. Rev. Neurosci.* **19,** 235–263
8. Craven, K. B., and Zagotta, W. N. (2006) CNG and HCN channels: two peas, one pod. *Annu. Rev. Physiol.* **68,** 375–401
9. Flynn, G. E., Johnson, J. P., Jr, and Zagotta, W. N. (2001) Cyclic nucleotide-gated channels: shedding light on the opening of a channel pore. *Nat. Rev. Neurosci.* **2,** 643–651
10. Johnson, J. P., Jr, and Zagotta, W. N. (2005) The carboxyl-terminal region of cyclic nucleotide-modulated channels is a gating ring, not a permeation path. *Proc. Natl. Acad. Sci. U.S.A.* **102,** 2742–2747
11. Chow, S. S., Van Petegem, F., and Accili, E. A. (2012) Energetics of cyclic AMP binding to HCN channel C terminus reveal negative cooperativity. *J. Biol. Chem.* **287,** 600–606
12. Hegle, A. P., Nazzari, H., Roth, A., Angoli, D., and Accili, E. A. (2010) Evolutionary emergence of N-glycosylation as a variable promoter of HCN channel surface expression. *Am. J. Physiol. Cell Physiol.* **298,** C1066–C1076
13. Jackson, H. A., Hegle, A., Nazzari, H., Jegla, T., and Accili, E. A. (2012) Asymmetric divergence in structure and function of HCN channel duplicates in *Ciona intestinalis. PLoS One* **7,** e47590
14. Jackson, H. A., Marshall, C. R., and Accili, E. A. (2007) Evolution and structural diversification of hyperpolarization-activated cyclic nucleotide-gated channel genes. *Physiol. Genomics* **29,** 231–245
15. Macri, V., and Accili, E. A. (2004) Structural elements of instantaneous and slow gating in hyperpolarization-activated cyclic nucleotide-gated channels. *J. Biol. Chem.* **279,** 16832–16846
16. Macri, V., Angoli, D., and Accili, E. A. (2012) Architecture of the HCN selectivity filter and control of cation permeation. *Sci. Rep.* **2,** 894
17. Macri, V., Nazzari, H., McDonald, E., and Accili, E. A. (2009) Alanine scanning of the S6 segment reveals a unique and cAMP-sensitive association between the pore and voltage-dependent opening in HCN channels. *J. Biol. Chem.* **284,** 15659–15667
18. Mistrík, P., Mader, R., Michalakis, S., Weidinger, M., Pfeifer, A., and Biel, M. (2005) The murine HCN3 gene encodes a hyperpolarization-activated cation channel with slow kinetics and unique response to cyclic nucleotides. *J. Biol. Chem.* **280,** 27056–27061
19. Qu, Y., Whitaker, G. M., Hove-Madsen, L., Tibbits, G. F., and Accili, E. A. (2008) Hyperpolarization-activated cyclic nucleotide-modulated 'HCN' channels confer regular and faster rhythmicity to beating mouse embryonic stem cells. *J. Physiol.* **586,** 701–716
20. Whitaker, G. M., Angoli, D., Nazzari, H., Shigemoto, R., and Accili, E. A. (2007) HCN2 and HCN4 isoforms self-assemble and co-assemble with equal preference to form functional pacemaker channels. *J. Biol. Chem.* **282,** 22900–22909
21. Lolicato, M., Nardini, M., Gazzarrini, S., Möller, S., Bertinetti, D., Herberg, F. W., Bolognesi, M., Martin, H., Fasolini, M., Bertrand, J. A., Arrigoni, C., Thiel, G., and Moroni, A. (2011) Tetramerization dynamics of C-terminal domain underlies isoform-specific cAMP gating in hyperpolarization-activated cyclic nucleotide-gated channels. *J. Biol. Chem.* **286,** 44811–44820

22. Xu, X., Vysotskaya, Z. V., Liu, Q., and Zhou, L. (2010) Structural basis for the cAMP-dependent gating in the human HCN4 channel. *J. Biol. Chem.* **285,** 37082–37091

23. Wainger, B. J., DeGennaro, M., Santoro, B., Siegelbaum, S. A., and Tibbs, G. R. (2001) Molecular mechanism of cAMP modulation of HCN pacemaker channels. *Nature* **411,** 805–810

24. Kim, C., Cheng, C. Y., Saldanha, S. A., and Taylor, S. S. (2007) PKA-I holoenzyme structure reveals a mechanism for cAMP-dependent activation. *Cell* **130,** 1032–1043

25. Taraska, J. W., Puljung, M. C., Olivier, N. B., Flynn, G. E., and Zagotta, W. N. (2009) Mapping the structure and conformational movements of proteins with transition metal ion FRET. *Nat. Methods* **6,** 532–537

26. Badireddy, S., Yunfeng, G., Ritchie, M., Akamine, P., Wu, J., Kim, C. W., Taylor, S. S., Qingsong, L., Swaminathan, K., and Anand, G. S. (2011) Cyclic AMP analog blocks kinase activation by stabilizing inactive conformation: conformational selection highlights a new concept in allosteric inhibitor design. *Mol. Cell. Proteomics* **10,** 10.1074/mcp.M110.004390

27. Kim, J. J., Casteel, D. E., Huang, G., Kwon, T. H., Ren, R. K., Zwart, P., Headd, J. J., Brown, N. G., Chow, D. C., Palzkill, T., and Kim, C. (2011) Co-crystal structures of PKG Iβ (92–227) with cGMP and cAMP reveal the molecular details of cyclic-nucleotide binding. *PLoS One* **6,** e18413

28. Delaglio, F., Grzesiek, S., Vuister, G. W., Zhu, G., Pfeifer, J., and Bax, A. (1995) Nmrpipe–a multidimensional spectral processing system based on unix pipes. *J. Biomol. NMR.* **6,** 277–293

29. Goddard, T. D., and Kneller, D. G. (0000) *SPARKY,* Version 3, University of California, San Francisco

30. Sattler, M., Schleucher, J., and Griesinger, C. (1999) Heteronuclear multidimensional NMR experiments for the structure determination of proteins in solution employing pulsed field gradients. *Prog. Nucl. Magn. Reson. Spectrosc.* **34,** 93–158

31. Eghbalnia, H. R., Bahrami, A., Wang, L., Assadi, A., and Markley, J. L. (2005) Probabilistic identification of spin systems and their assignments including coil-helix inference as output (PISTACHIO). *J. Biomol. NMR* **32,** 219–233

32. Mazhab-Jafari, M. T., Das, R., Fotheringham, S. A., SilDas, S., Chowdhury, S., and Melacini, G. (2007) Understanding cAMP-dependent allostery by NMR spectroscopy: comparative analysis of the EPAC1 cAMP-binding domain in its apo- and cAMP-bound states. *J. Am. Chem. Soc.* **129,** 14482–14492

33. Selvaratnam, R., VanSchouwen, B., Fogolari, F., Mazhab-Jafari, M. T., Das, R., and Melacini, G. (2012) The projection analysis of NMR chemical shifts reveals extended EPAC autoinhibition determinants. *Biophys. J.* **102,** 630–639

34. Selvaratnam, R., Chowdhury, S., VanSchouwen, B., and Melacini, G. (2011) Mapping allostery through the covariance analysis of NMR chemical shifts. *Proc. Natl. Acad. Sci. U.S.A.* **108,** 6133–6138

35. Akimoto, M., Selvaratnam, R., McNicholl, E. T., Verma, G., Taylor, S. S., and Melacini, G. (2013) Signaling through dynamic linkers as revealed by PKA. *Proc. Natl. Acad. Sci. U.S.A.* **110,** 14231–14236

36. Pawley, N. H., Koide, S., and Nicholson, L. K. (2002) Backbone dynamics and thermodynamics of *Borrelia* outer surface protein A. *J. Mol. Biol.* **324,** 991–1002

37. Cordier, F., Dingley, A. J., and Grzesiek, S. (1999) A doublet-separated sensitivity-enhanced HSQC for the determination of scalar and dipolar one-bond J-couplings. *J. Biomol. NMR* **13,** 175–180

38. Hansen, M. R., Mueller, L., and Pardi, A. (1998) Tunable alignment of macromolecules by filamentous phage yields dipolar coupling interactions. *Nat. Struct. Biol.* **5,** 1065–1074

39. Tugarinov, V., and Kay, L. E. (2005) Methyl groups as probes of structure and dynamics in NMR studies of high-molecular-weight proteins. *Chembiochem* **6,** 1567–1577

40. Battiste, J. L., and Wagner, G. (2000) Utilization of site-directed spin labeling and high-resolution heteronuclear nuclear magnetic resonance for global fold determination of large proteins with limited nuclear Overhauser effect data. *Biochemistry* **39,** 5355–5365

41. Thompson, J., and Baker, D. (2011) Incorporation of evolutionary information into Rosetta comparative modeling. *Proteins* **79,** 2380–2388

42. Vernon, R., Shen, Y., Baker, D., and Lange, O. F. (2013) Improved chemical shift based fragment selection for CS-Rosetta using Rosetta3 fragment picker. *J. Biomol. NMR* **57,** 117–127

43. van der Schot, G., Zhang, Z., Vernon, R., Shen, Y., Vranken, W. F., Baker, D., Bonvin, A. M., and Lange, O. F. (2013) Improving 3D structure prediction from chemical shift data. *J. Biomol. NMR* **57,** 27–35

44. Lange, O. F., Rossi, P., Sgourakis, N. G., Song, Y., Lee, H. W., Aramini, J. M., Ertekin, A., Xiao, R., Acton, T. B., Montelione, G. T., and Baker, D. (2012) Determination of solution structures of proteins up to 40 kDa using CS-Rosetta with sparse NMR data from deuterated samples. *Proc. Natl. Acad. Sci. U.S.A.* **109,** 10873–10878

45. Lange, O. F., and Baker, D. (2012) Resolution-adapted recombination of structural features significantly improves sampling in restraint-guided structure calculation. *Proteins* **80,** 884–895

46. Bouvignies, G., Vallurupalli, P., Hansen, D. F., Correia, B. E., Lange, O., Bah, A., Vernon, R. M., Dahlquist, F. W., Baker, D., and Kay, L. E. (2011) Solution structure of a minor and transiently formed state of a T4 lysozyme mutant. *Nature* **477,** 111–114

47. Warner, L. R., Varga, K., Lange, O. F., Baker, S. L., Baker, D., Sousa, M. C., and Pardi, A. (2011) Structure of the BamC two-domain protein obtained by Rosetta with a limited NMR data set. *J. Mol. Biol.* **411,** 83–95

48. Sgourakis, N. G., Lange, O. F., DiMaio, F., André, I., Fitzkee, N. C., Rossi, P., Montelione, G. T., Bax, A., and Baker, D. (2011) Determination of the structures of symmetric protein oligomers from NMR chemical shifts and residual dipolar couplings. *J. Am. Chem. Soc.* **133,** 6288–6298

49. Leaver-Fay, A., Tyka, M., Lewis, S. M., Lange, O. F., Thompson, J., Jacak, R., Kaufman, K., Renfrew, P. D., Smith, C. A., Sheffler, W., Davis, I. W., Cooper, S., Treuille, A., Mandell, D. J., Richter, F., Ban, Y. E., Fleishman, S. J., Corn, J. E., Kim, D. E., Lyskov, S., Berrondo, M., Mentzer, S., Popović, Z., Havranek, J. J., Karanicolas, J., Das, R., Meiler, J., Kortemme, T., Gray, J. J., Kuhlman, B., Baker, D., and Bradley, P. (2011) ROSETTA3: an object-oriented software suite for the simulation and design of macromolecules. *Methods Enzymol.* **487,** 545–574

50. Raman, S., Lange, O. F., Rossi, P., Tyka, M., Wang, X., Aramini, J., Liu, G., Ramelot, T. A., Eletsky, A., Szyperski, T., Kennedy, M. A., Prestegard, J., Montelione, G. T., and Baker, D. (2010) NMR structure determination for larger proteins using backbone-only data. *Science* **327,** 1014–1018

51. Thompson, J. M., Sgourakis, N. G., Liu, G., Rossi, P., Tang, Y., Mills, J. L., Szyperski, T., Montelione, G. T., and Baker, D. (2012) Accurate protein structure modeling using sparse NMR data and homologous structure information. *Proc. Natl. Acad. Sci. U.S.A.* **109,** 9875–9880

52. Shen, Y., Lange, O., Delaglio, F., Rossi, P., Aramini, J. M., Liu, G., Eletsky, A., Wu, Y., Singarapu, K. K., Lemak, A., Ignatchenko, A., Arrowsmith, C. H., Szyperski, T., Montelione, G. T., Baker, D., and Bax, A. (2008) Consistent blind protein structure generation from NMR chemical shift data. *Proc. Natl. Acad. Sci. U.S.A.* **105,** 4685–4690

53. Zong, X., Krause, S., Chen, C. C., Krüger, J., Gruner, C., Cao-Ehlker, X., Fenske, S., Wahl-Schott, C., and Biel, M. (2012) Regulation of hyperpolarization-activated cyclic nucleotide-gated (HCN) channel activity by cCMP. *J. Biol. Chem.* **287,** 26506–26512

54. Shi, L., Traaseth, N. J., Verardi, R., Gustavsson, M., Gao, J., and Veglia, G. (2011) Paramagnetic-based NMR restraints lift residual dipolar coupling degeneracy in multidomain detergent-solubilized membrane proteins. *J. Am. Chem. Soc.* **133,** 2232–2241

55. Tonelli, M., Masterson, L. R., Cornilescu, G., Markley, J. L., and Veglia, G. (2009) One-sample approach to determine the relative orientations of proteins in ternary and binary complexes from residual dipolar coupling measurements. *J. Am. Chem. Soc.* **131,** 14138–14139

56. Zhou, L., and Siegelbaum, S. A. (2007) Gating of HCN channels by cyclic nucleotides: residue contacts that underlie ligand binding, selectivity, and efficacy. *Structure* **15,** 655–670

57. Zhou, L., Olivier, N. B., Yao, H., Young, E. C., and Siegelbaum, S. A. (2004) A conserved tripeptide in CNG and HCN channels regulates ligand gating by controlling C-terminal oligomerization. *Neuron* **44,** 823–834

58. Ulens, C., and Siegelbaum, S. A. (2003) Regulation of hyperpolarization-activated HCN channels by cAMP through a gating switch in binding domain symmetry. *Neuron* **40,** 959–970

59. Flynn, G. E., Black, K. D., Islas, L. D., Sankaran, B., Zagotta, W. N. (2007) Structure and rearrangements in the carboxy-terminal region of SpIH

channels. *Structure* **15,** 671–682

60. Bruystens, J. G., Wu, J., Fortezzo, A., Kornev, A. P., Blumenthal, D. K., and Taylor, S. S. (2014) PKA RIα homodimer structure reveals an intermolecular interface with implications for cooperative cAMP binding and Carney complex disease. *Structure* **22,** 59–69

61. Ilouz, R., Bubis, J., Wu, J., Yim, Y. Y., Deal, M. S., Kornev, A. P., Ma, Y., Blumenthal, D. K., and Taylor, S. S. (2012) Localization and quaternary structure of the PKA RIβ holoenzyme. *Proc. Natl. Acad. Sci. U.S.A.* **109,** 12443–12448

62. Masterson, L. R., Cheng, C., Yu, T., Tonelli, M., Kornev, A., Taylor, S. S., and Veglia, G. (2010) Dynamics connect substrate recognition to catalysis in protein kinase A. *Nat. Chem. Biol.* **6,** 821–828

63. Masterson, L. R., Shi, L., Metcalfe, E., Gao, J., Taylor, S. S., and Veglia, G. (2011) Dynamically committed, uncommitted, and quenched states encoded in protein kinase A revealed by NMR spectroscopy. *Proc. Natl. Acad. Sci. U.S.A.* **108,** 6969–6974

64. Anand, G. S., Krishnamurthy, S., Bishnoi, T., Kornev, A., Taylor, S. S., and Johnson, D. A. (2010) Cyclic AMP- and (Rp)-cAMPS-induced conformational changes in a complex of the catalytic and regulatory (RIα) subunits of cyclic AMP-dependent protein kinase. *Mol. Cell. Proteomics* **9,** 2225–2237

65. Kelkar, D. S., Kumar, D., Kumar, P., Balakrishnan, L., Muthusamy, B., Yadav, A. K., Shrivastava, P., Marimuthu, A., Anand, S., Sundaram, H., Kingsbury, R., Harsha, H. C., Nair, B., Prasad, T. S., Chauhan, D. S., Katoch, K., Katoch, V. M., Kumar, P., Chaerkady, R., Ramachandran, S., Dash, D., and Pandey, A. (2011) Proteogenomic analysis of *Mycobacterium tuberculosis* by high resolution mass spectrometry. *Mol. Cell. Proteomics* 10.1074/mcp.M111.011627

66. Huang, G. Y., Kim, J. J., Reger, A. S., Lorenz, R., Moon, E. W., Zhao, C., Casteel, D. E., Bertinetti, D., Vanschouwen, B., Selvaratnam, R., Pflugrath, J. W., Sankaran, B., Melacini, G., Herberg, F. W., and Kim, C. (2014) Structural basis for cyclic-nucleotide selectivity and cGMP-selective activation of PKG I. *Structure* **22,** 116–124

67. McNicholl, E. T., Das, R., SilDas, S., Taylor, S. S., and Melacini, G. (2010) Communication between tandem cAMP binding domains in the regulatory subunit of protein kinase A-Iα as revealed by domain-silencing mutations. *J. Biol. Chem.* **285,** 15523–15537

68. Das, R., Chowdhury, S., Mazhab-Jafari, M. T., Sildas, S., Selvaratnam, R., and Melacini, G. (2009) Dynamically driven ligand selectivity in cyclic nucleotide binding domains. *J. Biol. Chem.* **284,** 23682–23696

69. Abu-Abed, M., Das, R., Wang, L., and Melacini, G. (2007) Definition of an electrostatic relay switch critical for the cAMP-dependent activation of protein kinase A as revealed by the D170A mutant of RIα. *Proteins* **69,** 112–124

70. Selvaratnam, R., Mazhab-Jafari, M. T., Das, R., and Melacini, G. (2012) The auto-inhibitory role of the EPAC hinge helix as mapped by NMR. *PLoS One* **7,** e48707

71. Selvaratnam, R., Akimoto, M., VanSchouwen, B., and Melacini, G. (2012) cAMP-dependent allostery and dynamics in Epac: an NMR view. *Biochem. Soc. Trans.* **40,** 219–223

72. VanSchouwen, B., Selvaratnam, R., Fogolari, F., and Melacini, G. (2011) Role of dynamics in the auto-inhibition and activation of the exchange protein directly activated by cyclic AMP (EPAC). *J. Biol. Chem.* **286,** 42655–42669

73. Gavina, J. M., Mazhab-Jafari, M. T., Melacini, G., and Britz-McKibbin, P. (2009) Label-free assay for thermodynamic analysis of protein-ligand interactions: a multivariate strategy for allosteric ligand screening. *Biochemistry* **48,** 223–225

74. Das, R., Mazhab-Jafari, M. T., Chowdhury, S., SilDas, S., Selvaratnam, R., and Melacini, G. (2008) Entropy-driven cAMP-dependent allosteric control of inhibitory interactions in exchange proteins directly activated by cAMP. *J. Biol. Chem.* **283,** 19691–19703

75. Rehmann, H., Wittinghofer, A., and Bos, J. L. (2007) Capturing cyclic nucleotides in action: snapshots from crystallographic studies. *Nat. Rev. Mol. Cell Biol.* **8,** 63–73

76. Schünke, S., Stoldt, M., Lecher, J., Kaupp, U. B., and Willbold, D. (2011) Structural insights into conformational changes of a cyclic nucleotide-binding domain in solution from *Mesorhizobium loti* K1 channel. *Proc. Natl. Acad. Sci. U.S.A.* **108,** 6121–6126

77. Nussinov, R. (2013) The spatial structure of cell signaling systems. *Phys. Biol.* **10,** 045004

78. Nussinov, R., Tsai, C. J., and Csermely, P. (2011) Allo-network drugs: harnessing allostery in cellular networks. *Trends Pharmacol. Sci.* **32,** 686–693

79. Nussinov, R., Tsai, C. J., and Ma, B. (2013) The underappreciated role of allostery in the cellular network. *Annu. Rev. Biophys.* **42,** 169–189

80. Boulton, S., Akimoto, M., VanSchouwen, B., Moleschi, K., Selvaratnam, R., Giri, R., and Melacini, G. (2014) Tapping the translation potential of cAMP signalling: molecular basis for selectivity in cAMP agonism and antagonism as revealed by NMR. *Biochem. Soc. Trans.* **42,** 302–307

81. Ming, D., and Brüschweiler, R. (2004) Prediction of methyl-side chain dynamics in proteins. *J. Biomol. NMR* **29,** 363–368

82. Shen, Y., Delaglio, F., Cornilescu, G., and Bax, A. (2009) TALOS+: A hybrid method for predicting protein backbone torsion angles from NMR chemical shifts. *J. Biomol. NMR* **44,** 213–223